Water Resources Research

RESEARCH ARTICLE
10.1029/2021WR031837

Fine-Sediment Erosion and Sediment-Ribbon Morphodynamics in Coarse-Grained Immobile Beds

Michele Trevisson[1] and **Olivier Eiff**[1]

[1]Institute for Hydromechanics, Karslruhe Institute of Technology, Karlsruhe, Germany

Key Points:

- Four erosive regimes are identified: drag sheltering, turbulence-enhancement, wake-interference sheltering and skimming-flow sheltering
- Secondary currents influence the momentum redistribution but the erosive behavior is controlled by the protrusion of the immobile grains
- The sediment-ribbon spacing is about 1.3 effective water depths

Correspondence to:
M. Trevisson,
michele.trevisson@kit.edu

Citation:
Trevisson, M., & Eiff, O. (2022). Fine-sediment erosion and sediment-ribbon morphodynamics in coarse-grained immobile beds. *Water Resources Research*, *58*, e2021WR031837. https://doi.org/10.1029/2021WR031837

Received 16 DEC 2021
Accepted 28 OCT 2022
Corrected 8 DEC 2022

This article was corrected on 8 DEC 2022. See the end of the full text for details.

Abstract In rivers, fine sediments are often transported over immobile coarse grains. With low sediment supply, they tend to aggregate in longitudinal ribbons. Yet, the long-term evolution of such ribbons and the influence of immobile grains on the erosion of fine sediments are still not well understood. Flume experiments without sediment supply were therefore performed to investigate the erosion of an initially uniform fine-sediment bed covering an immobile bed of staggered spheres through topographic and flow measurements. The topographic measurements yielded the spheres' protrusion above the fine sediment (P) and revealed long-lived ribbons with ridges and troughs. The ridges are the main long-term sediment source as the troughs are quickly eroded to a stable bed level resulting from the spheres' sheltering. The ridges stabilize with a spacing of 1.3 effective water depths, their number resulting from the integer number of wavelengths fitting into the effective channel width which excludes side-wall accumulations. The ridges' erosion is damped by the local upflow of secondary current cells, which displaces the strongest sweep events above the bed. The upflow intensity is controlled by the ridges' height for low P, while for high P by the lateral roughness heterogeneity. The trends in erosion rates over ridges and troughs are similar and characterized by the following sequence of four regimes with increasing P: a *drag sheltering*, a *turbulence-enhancement*, a *wake-interference sheltering*, and a *skimming-flow sheltering* regime. The critical P levels at the transitions are independent of the flow above the canopy, depending only on the geometrical configuration of the immobile bed.

1. Introduction

The transport of fine sediments over an immobile substrate composed of coarser grains is frequently observed in both aeolian and river environments. Typical riverine examples which are the target of this study, are bimodal sand-gravel bed rivers where the prevalent flow conditions below bankfull discharge are characterized by partial sediment transport with the coarser sediments, i.e., gravel or cobbles, building an immobile armor layer and with the fines being transported as bedload on the bed surface (Ashworth & Ferguson, 1989; Kleinhans, 2002; Vericat et al., 2008; Wilcock & McArdell, 1993). Overall, the effect of coarse immobile roughness elements on the underlying fine-sediment surface has been characterized mostly from a hydrodynamic point of view; the immobile roughness elements increase the drag on the flow causing increased bed resistance (Rickenmann & Recking, 2011) and a reduction of the shear stress acting on the underlying surface (Le Bouteiller & Venditti, 2015; Marshall, 1971; Raupach, 1992; Yager et al., 2007). At the same time, the coherent structures shed by the immobile roughness elements, such as horseshoe vortices developing in their stoss side and arc-shaped shear layers encompassing a recirculation region in their lee, induce highly heterogeneous shear stress conditions (Fang et al., 2017; Papanicolaou et al., 2012; Pattenden et al., 2005; Raus et al., 2019). These create localized scour regions and sediment shadows in the stoss and lee side of the immobile roughness elements (Dixen et al., 2013; Euler & Herget, 2012; McKenna Neuman et al., 2013). The fine sediments being transported over an immobile rough layer can experience as such both increased and decreased shear stress conditions, so that the impact of the immobile roughness elements on the erosion and transport of fine sediments is still not well understood (Raus et al., 2019; Yager et al., 2007).

Differences in fine-sediment transport and erosion rates over rough immobile substrates as compared to uniform fine sediment beds (i.e., composed of sediments of approximately the same sediment size) have been ascribed to two main parameters: the planar density and the protrusion of the roughness elements above the underlying fine-sediment bed (Grams & Wilcock, 2007; Yager et al., 2007). Early studies on aeolian sediment transport by Gillette and Stockton (1989) and Iversen et al. (1991) analyzed the impact of immobile roughness elements with a fixed level of exposure on grain saltation. They observed that with increasing planar density of the roughness elements, the shear stress to obtain the same particle flux increases. Similarly, the aeolian laboratory and field

studies by Gillies et al. (2006) and Al-Awadhi and Willetts (1999) observed a decrease in the saltation flux as the planar density of arrays of cylinders increased. Gillies et al. (2006) associated this protection effect to the trapping of saltating particles in the lee side of immobile roughness elements. Open-channel laboratory studies with immobile boulders (Ghilardi et al., 2014; Papanicolaou et al., 2011) or large coarse grains (Yager et al., 2007) confirmed this reduction in the fine-sediment transport capacity of the flow with decreasing roughness element spacing as compared to uniform beds.

The influence of immobile-grain protrusion on the fine-sediment transport was first highlighted by Nickling and McKenna Neumann (1995) and McKenna Neuman and Nickling (1995), who analyzed the wind-induced transport of fine sediments from an immobile bed of spheres initially covered with sediments. They observed that the sand flux increases as soon as the spheres start to protrude from the bed, eventually reducing to zero as the exposure of the spheres increases. A similar behavior was observed also by Grams and Wilcock (2007) who studied the entrainment of fine sand into suspension over a bed composed of gravel-sized fixed hemispheres in open-channel flows. They assessed that for sand-bed elevations higher than 50% of the hemisphere's radius R the entrainment rates increase while below they are significantly reduced. Few measurements were collected for sand bed levels higher than $0.3R$, though. In the open-channel studies by Kuhnle et al. (2013) and Wren and Kuhnle (2014) on the transport of sand as mixed bedload and suspension over immobile gravel and cobble, the initial increase and following decrease in sand transport rates with decreasing sand-bed content was associated with an increase of the total bed shear stress, the decrease suggesting that the immobile roughness elements shelter the fine sediment. The initial increase in sediment transport rates has not been observed by Yager et al. (2007), however, who studied the sediment transport in a steep open-channel over immobile spheres with different planar densities. They found that the sediment transport simply decreases with increasing sphere's protrusion.

The evolution of the erosion rates of fine sediments from a gravel bed was investigated, to our knowledge, only recently by Stradiotti et al. (2020) who highlight a decreasing trend in erosion rates with decreasing fine-sediment level. Yet, oscillations in the erosion rates were observed for low protrusion of the gravel grains suggesting temporary increase in erosion rates as similarly observed for the sediment transport rates (e.g., Grams & Wilcock, 2007; Nickling & McKenna Neumann, 1995). However, this temporary increase in erosion rates does not lead to erosion rates higher than the ones being observed for a uniform fine sediment bed, in contrast to the observations of Grams and Wilcock (2007) and Nickling and McKenna Neumann (1995) for the sediment transport rates.

The experimental observations so far suggest that immobile grains exert two competing effects on the mobile sediment: they reduce or enhance the sediment transport and erosion rates of the fine sediments, with the planar density and the protrusion level potentially having opposite effects for certain ranges of fine-sediment content. Yet, the available studies do not provide a clear description of the factors and processes governing this behavior, and thus no reliable predictive model. It is therefore not surprising that Yager et al. (2007) and Stradiotti et al. (2020) who develop predictive equations for the entrainment rates into suspension and erosion of fine sediments in the presence of immobile roughness elements, respectively, consider only the reducing effect of both quantities, while the enhancement is neglected.

The limited availability of fine sediments in the presence of immobile grains without upstream sediment supply influences the type of bedforms which develop (Grams & Wilcock, 2014; Kleinhans et al., 2002). In particular, sediment ribbons are observed in natural sand-gravel bed rivers (Culbertson, 1967; Ferguson et al., 1989; Karcz, 1966; Kleinhans et al., 2002) and in laboratory investigations on bimodal sediment mixtures (McLean, 1981; McLelland et al., 1999; Nezu & Nakagawa, 1989). The ribbons appear only for lower availability, while for higher availability, barcans and dunes form (Kleinhans et al., 2002). Sediment ribbons are also observed in uniform sediment beds (Hirano & Ohmoto, 1988; Nezu et al., 1988; Wolman & Brush, 1961) where they stem from a limitation of the transport capacity. In this case, the ribbons develop for shear stress conditions up to three times the critical shear stress for grain motion (Hirano & Ohmoto, 1988).

Sediment ribbons are characterized by variations in bed topography with flow-aligned ridges and troughs (Hirano & Ohmoto, 1988; Wolman & Brush, 1961), on top of which a variation in the bed texture can be also observed in sediment mixtures, with coarser grains present in the troughs and finer grains on the ridges (McLean, 1981; McLelland et al., 1999; Nezu & Nakagawa, 1989). So far, the morphology of sediment ribbons has been studied quantitatively only under stationary, fully-developed bed conditions. The above cited studies focused essentially on the lateral ridge spacing and find a large scatter between one and three water depths. The development and morphological evolution of sediment ribbons has been described only qualitatively, for uniform beds by Hirano

and Ohmoto (1988) and with immobile grains by McLean (1981), Grams and Wilcock (2014), Raus (2019). One exception is the recent DNS study of Scherer et al. (2022), who found and described the development of ribbons on an initially flat bed of uniform spherical particles, albeit in an infinitely large open-channel flow for bulk Reynolds numbers below 9,000. They observed that the ridges form almost instantaneously with their spacing decreasing and height increasing over time before eventually stabilizing.

From a morphodynamic point of view, sediment ribbons result from the interaction with secondary currents (Nezu et al., 1988). Typical flow patterns developing over sediment ribbons are characterized by upflow over the ridges and downflow over the troughs, corresponding to low and high speed regions, respectively (Nezu et al., 1988; Scherer et al., 2022). Furthermore, higher shear stress conditions are present over the troughs than over the ridges, leading to differential erosion of the sediment bed (McLelland et al., 1999; Nezu & Nakagawa, 1989; Scherer et al., 2022). At the same time, the topography of the sediment ribbons feeds back on the intensity of the secondary currents, with studies on fixed artificial ridges or roughness stripes showing that the secondary currents are mainly influenced by the ridges' height, width and spacing, and lateral roughness heterogeneity (Medjnoun et al., 2020; Nezu & Nakagawa, 1984; Vanderwel & Ganapathisubramani, 2015; Wang & Cheng, 2006; Willingham et al., 2014). However, to our knowledge, no study has analyzed how the secondary currents are modified during the development of ribbons with uniform mixtures in the presence of coarse immobile grains.

In light of the open issues raised, concerning both the erosive behavior and bedforms with immobile grains present, we propose a controlled laboratory study in a tilting flume to examine the long-time evolution of the erosion of fine sediments from an immobile bed of spheres, without upstream sediment supply and for mid- to low-land fluvial conditions. Two main research questions are addressed: first, how does the protrusion of the immobile grains affect the erosion rates of the fine sediments? We hypothesize that transitions in erosive behavior occur at specific protrusion levels. Second, how does the sediment ribbons' morphology evolve along with the coupled secondary currents? We hypothesize that the presence of roughness elements does not influence the lateral spacing of the sediment ribbons but rather that the intensity of the secondary currents is affected by the associated lateral roughness heterogeneity and by the ribbons' morphology to a different degree as the protrusion of the immobile grains changes.

To analyze the bed morphology both at the bedform and roughness scale, the topography of the eroding fine-sediment bed was measured continuously with an image-based topographic technique from above at two streamwise locations, yielding the temporal evolution of the bedform morphology and of the local erosion rate. The flow was investigated via a planar Particle Image Velocimetry (PIV) technique in two streamwise-oriented vertical planes above the spheres' top, yielding information about the secondary currents at selected times during the evolution of the bed.

The experimental setup and methodology are given in Section 2. The results are given in Section 3 and are organized as follows: A global description of the bed morphology via the bed level (the spheres' protrusion) measurements spanning the width of the channel is presented in Section 3.1. The extraction of the morphological features and spacings of the sediment ribbons from the protrusion measurements is presented in Section 3.2. Next, the protrusion level measurements are used to determine the erosive behavior of the troughs and ridges of the detected ribbons in Section 3.3. Finally, the mean and turbulence profiles computed from the PIV measurements above the troughs and ridges are presented in Section 3.4. These results are discussed in Section 4 before concluding in Section 5.

2. Methods

2.1. Experimental Setup

The experiments were conducted at the Institute of Hydromechanics at the Karlsruhe Institute of Technology in a 9.2 m long, 30 cm wide and 32 cm high tilting flume (Figure 1a) with a downstream weir to adjust water levels. A horizontal convex grid installed in the entrance tank followed by a contraction ensured low turbulence and quasi-uniform flow conditions at the inlet. The flow rate Q was measured with a calibrated venturi meter and the water levels were measured through a point gauge with a precision of 0.1 mm attached to a movable carriage. The experiments were performed under sediment-supply-limited conditions, i.e., with no upstream sediment feed. The sediments were collected in a settling tank beneath the weir.

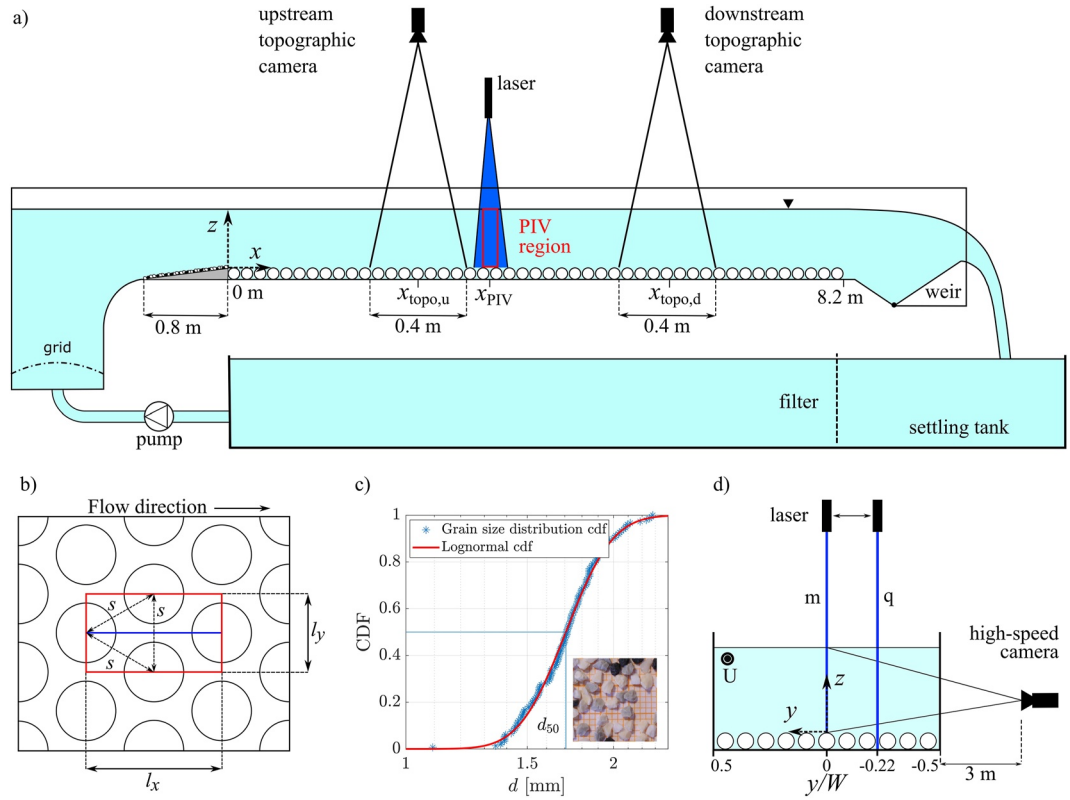

Figure 1. (a) Flume setup. See Table 3 for the values of the positions of the measurement systems. (b) Staggered pattern of spheres with the reference pattern highlighted in red with $l_x = 4.54$ cm and $l_y = s = 2.62$ cm. The blue line indicates the laser-sheet position; (c) Grain-size distribution and fitted lognormal cumulative density function (CDF); insert: plastic granulates over graph paper with 1 mm mesh size; (d) Cross-sectional view with the Particle Image Velocimetry (PIV) setup.

The coordinate system was chosen as follows: x = streamwise direction with origin at the beginning of the sediment bed, i.e., 0.8 m downstream of the inlet at the end of a 1.7° inclined ramp, y = spanwise direction with origin in the center of the flume, z = vertical direction with origin at the top of the spheres constituting the immobile rough bed (Figure 1a).

2.2. Bed and Sediment Properties

The bed was designed to analyze the effect of large immobile roughness elements on the erosion of fine sediments, as observed in sand-gravel bed rivers. Field studies on various gravel-bed rivers have reported that the ratio between the immobile grain fraction, represented by the d_{90} of the bed surface, to the d_{50} of the transported bedload is of the order of 4–100 (Carling et al., 2000; Ferguson et al., 1989; Lenzi, 2004; Pitlick, 1993). Here, the size ratio between immobile roughness elements and fine mobile sediments is equal to 11.6, close to the one observed by Kleinhans et al. (2002) in the bimodal sediment bed of the river Waal, a tributary of the river Rhine. The immobile grains were made of white polyurethane spheres with a diameter $D = 2R = 2$ cm. The spheres were glued to glass plates positioned on the flume's bed, in a staggered symmetric pattern (Figure 1b), symmetrically with respect to the walls, and covering the entire length of the flume (Figure 1a). The reference pattern (Figure 1b) has a porosity of $\phi = 0.65$, similar to the upper layer of static armored gravel beds (Aberle, 2007). A diagonal sphere-spacing to diameter ratio of $s/D = 1.31$, higher than 1, was chosen to avoid fine sediment clogging in the bed interstices. The planar density of the pattern $\lambda_p = S_p/S_r = 0.53$ for half-eroded spheres (where S_p is the planar area of the spheres in the reference pattern and $S_r = l_x l_y$ the total area of the pattern with $l_x = 4.54$ cm and $l_y = 2.62$ cm) defines skimming flow conditions (Grimmond & Oke, 1999).

The fine sediments were made of plastic granulate consisting of urea, melamine and phenol with a specific weight $\rho_s = 1.49$ g/cm^3 and a porosity $\phi_s = 0.45$. The grain size distribution was determined by measuring the

Table 1
Flow Parameters of the Experiments

Exp.		θ (–)	A (–)	Q (l/s)	i (%)	H (cm/s)	R_H^c (cm)	u_{*R^c} (cm/s)	u_{*H} (cm/s)	U (cm/s)	Re^* (–)	Re (–)	Fr (–)	T_e (h)
1a	θlAm	0.11	4.6	5.0	0.16	6.50	5.8	3.0	3.2	26	51	16,600	0.32	71
1b	θlAm	0.11	4.6	5.0	0.16	6.43	5.8	3.0	3.2	26	51	16,600	0.33	92
2	θmAm	0.15	4.4	6.1	0.20	6.85	6.1	3.5	3.7	30	59	20,300	0.36	44
3	θhAm	0.18	4.4	7.4	0.25	6.84	6.1	3.8	4.0	36	66	24,600	0.44	70
4	θlAh	0.12	6.5	3.0	0.23	4.59	4.3	3.1	3.2	22	53	10,000	0.32	67
5a	θlAl	0.12	2.9	9.4	0.12	10.26	8.6	3.2	3.5	31	54	31,300	0.30	66
5b	θlAl	0.12	2.9	9.4	0.12	10.35	8.6	3.2	3.5	30	54	31,300	0.30	43
		±0.01	±0.1	±0.5	±0.01	±0.05	±0.1	±0.1	±0.1	±2				

Note. Shields parameter $\theta = u_{*R^c}^2 / (g\Delta d_{50})$, aspect ratio $A = W/H$, flow rate Q, slope i, water depth H, hydraulic radius with side-wall correction R_h^c, shear velocity $u_{*R^c} = \sqrt{gR_h^c i}$ based on the hydraulic radius R_h^c, shear velocity $u_{*H} = \sqrt{gHi}$ based on the water depth H, bulk velocity $U = Q/(WH)$, particle Reynolds number $Re^* = u_{*R^c} d_{50}/\nu$, bulk Reynolds number $Re = HU/\nu$, Froude number $Fr = U/\sqrt{gH}$, time duration of the experiment T_e.

intermediate principle b-axis of the grains on the basis of the minor axis of the ellipse which best fits each grain (Graham et al., 2005), as done in the analysis of river sediments (Church et al., 1987). It was measured by image sampling a large amount of grains scattered over a black background after verifying that no overlap between grains was present. It was then ascertained that the grain size distribution follows a lognormal probability density function (Figure 1c) as for natural fine sediments (Dey & Das, 2012), by applying the test of Pearson with a level of significance $\alpha = 0.05$ (Bendat & Piersol, 2010). The grain size distribution was characterized by a median diameter $d_{50} = 1.72$ mm and by a geometric standard deviation $\sigma_g = (d_{84}/d_{16})^{0.5} = 1.13$. Since $\sigma_g < 1.4$, the plastic granulate was classified as well-graded and uniform (Dey, 2014). In this manner, the bimodal behavior of the bed arised only from the interaction between the spheres and the fine sediments, given their large size ratio.

The bed was prepared to reproduce an immobile gravel bed being temporarily covered by fine sediments due to an increased sediment supply from upstream. Before each experiment, the spheres were therefore covered, over the whole length of the flume, by a layer of plastic granulate 3 cm thick, i.e., 1 cm over the top of the spheres. The bed was then mechanically screeded to create a uniform, flat surface to ensure reproducible initial experimental conditions and to reduce roughness anisotropies.

After screeding, the bed was filled with water up to the top of the sediment layer to flush remaining air out. The experiments were started by carefully increasing the flow rate to the final working conditions in order to avoid an abrupt flushing of the fine sediments and to start reworking the bed. Furthermore, to avoid increased erosion at the beginning of the sediment bed due to a jump of the incoming flow from the flume bed level to the sediment bed level, the aforementioned 0.8 m long ramp, inclined by 1.7°, was installed at the channel entrance with the downstream end flush with the top of the spheres (Figure 1a). The surface of the ramp was glued with a layer of the fine sediments in order to trigger an early development of the rough boundary layer.

2.3. Flow Parameters

The flow parameters were chosen to study, first, the erosion of the fine sediments under bedload conditions with increasing bed shear stress and second, the dependency of developing longitudinal bedforms on the flow depth. A total of seven experiments were performed under uniform flow conditions by varying two parameters: the total shear stress, expressed in terms of the Shields parameter $\theta = u_{*R^c}^2 / (g\Delta d_{50})$ and the water depth, expressed in terms of the channel-flow aspect ratio $A = W/H$, see Table 1. Here, $\Delta = 0.49$ is the relative density of the fine sediments, W is the width of the channel and H is a reference water depth with respect to the spheres' top ($z = 0$). The reference shear velocity u_{*R^c} is obtained from the integral momentum balance for a uniform flow with $u_{*R^c} = \sqrt{gR_H^c i}$, where i is the channel slope and R_H^c the hydraulic radius referred to the fine-sediment bed and obtained from the side-wall correction by Chiew and Parker (1994). $\rho u_{*R^c}^2$ represents, therefore, the mean bed shear stress of the uniform fine sediment at the level of the spheres' top.

Table 2
Parametric Concept for the Seven Experiments in Table 1

			A		
			l (≈2.9)	*m* (≈4.6)	*h* (≈6.5)
	l	(≈0.11)	5a/b	1a/b	4
θ	*m*	(≈0.15)	–	2	–
	h	(≈0.18)	–	3	–

Note. *l*, *m* and *h* indicate low, medium and high *A* and θ values, respectively.

The erosive conditions of the bed were defined by imposing values of the Shields parameter θ about 3.3–5 times the critical Shields parameter $\theta_{cr} = 0.033$ of the fine sediments. θ_{cr} was determined by the explicit relationship by Wu and Wang (1999) which relates θ_{cr} to the non-dimensional particle parameter $D_* = d_{50}\left(\Delta g/\nu^2\right)^{1/3}$. The θ-values correspond to flow conditions encountered in natural sand-gravel bed rivers, for which selective sediment transport takes place with the coarsest sediment fractions remaining mostly immobile, usually for low flow conditions (Carling et al., 2000; Kleinhans et al., 2002; Powell et al., 2001). The Shields parameters investigated are above the threshold for the development of sediment ribbons in uniform fine-sediment beds, equal to $3\theta_{cr}$ (Hirano & Ohmoto, 1988), in order to assess whether sediment ribbons can develop above this threshold in the presence of immobile roughness elements. A total of three Shields parameters were selected with increasing magnitude: low ($\theta \approx 0.11$), medium ($\theta \approx 0.15$) and high ($\theta = 0.18$). These values are low enough to yield only bedload as given by the suspension criteria of Bagnold (1966); Sumer (1986); Bose and Dey (2013) and as verified visually.

To analyze the influence of the secondary currents on the development of sediment ribbons, three aspect ratios with low ($A \approx 2.9$), medium ($A \approx 4.6$) and high ($A \approx 6.5$) magnitude were investigated. These were selected to be below, equal to and above the critical aspect ratio $A = 5$ identified by Nezu and Rodi (1985) to discriminate fully three dimensional from quasi two-dimensional open-channel flows over smooth beds. The highest aspect ratio $A = 6.5$ which is not significantly higher than $A = 5$, was selected to avoid low submergence effects (Rouzes et al., 2019), present if the water depth becomes comparable to the size of the protruding spheres.

Table 2 illustrates the parametric concept of the experiments, each experiment being associated with a Shields parameter and an aspect ratio of low (*l*), medium (*m*) or high (*h*) magnitude. Accordingly, in Table 1, the experiments were given acronyms with θ and *A* referring to the Shields parameter and the aspect ratio, respectively. As seen in Table 2, Exp. 1a/b (θlAm), Exp. 2 (θmAm), and Exp. 3 (θhAm) were performed with the same medium aspect ratio ($A \approx 4.6$) and with increasing Shields parameter while Exp. 5a/b (θlAl), Exp. 1a/b (θlAm), and Exp. 4 (θlAh) were performed with the same low Shields parameter ($\theta \approx 0.11$) and with increasing aspect ratio. Exp. 1b and Exp. 5b were performed under the same conditions as Exp. 1a and Exp. 5a, respectively, to assess, whether the experiments were reproducible and to perform measurements of the velocity field (see Section 2.4.2).

For each experimental configuration, in order to avoid lengthy adjustments with the mobile bed to set the desired shear stress and flow depth, the slope *i* was set via $u_{*H} = \sqrt{gHi}$, i.e., the maximum shear velocity acting on the bed based on the water depth. To estimate the necessary flow rate *Q* using the Darcy-Weisbach equation for a uniform flow, the friction factor was computed with the standard logarithmic friction law for the desired flow depth *H* with an equivalent sand-roughness equal to d_{50} for uniform sediment (Kironoto & Graf, 1995; Powell, 2014). Then, pre-experiments for each configuration were performed with a mobile fine-sediment bed to adjust the flow rate *Q* and the water depth *H* (measured every meter along the flume and adjusted via the weir position) to obtain effectively uniform flow conditions, defining the flow conditions in Table 1. It should be noted that during the experiments, the water level was monitored every half hour and was found to remain constant and uniform. The experiments lasted between 2 and 4 days (Table 1) and were run continuously with no interruptions.

2.4. Measurement Configurations

The temporal evolution of the bed topography was measured via a topographic system with a top-viewing camera for the measurement of the spheres' planar area (Section 2.4.1) as in Nickling and McKenna Neumann (1995) and Raus (2019), and the flow field above the spheres was measured by a 2D planar PIV system (Section 2.4.2). While the topographic measurements were performed without interruption over the entire duration of all experiments, the PIV measurements were performed, for efficiency, at three selected times during Exp. 1b and 5b only.

The measurements were performed at distances downstream of the inlet sufficient for the full development of the boundary layer, given by the semi-empirical relationship proposed by Monin and Yaglom (1971) with the coefficient by Nikora et al. (1998) for rough boundary layer growth: $L_{BL} = HU/(0.33u_{*R^c})$. Table 3 summarizes L_{BL} for the different experiments as well as the measurement locations of the topographic and PIV systems.

Table 3
Boundary-Layer Development Length L_{BL} and Location of the Topographic and Particle Image Velocimetry (PIV) Systems

Exp.	1a	1b	2	3	4	5a	5b
L_{BL} (m)	1.70	1.70	1.80	1.90	1.00	2.90	2.90
$x_{\text{topo,u}}$ (m)	3.35	2.70	3.35	3.35	3.35	3.35	2.70
$x_{\text{topo,d}}$ (m)	5.80	5.80	5.80	5.80	5.80	5.80	5.80
x_{PIV} (m)		3.70					3.70

Note. L_{BL} is based on the Monin and Yaglom (1971) formula with coefficient by Nikora et al. (1998). The indices u and d refer to the upstream and downstream location of the topographic system.

2.4.1. Topographic Measurements

The mean protrusion height k around each sphere (Figure 2a) was determined by measuring the exposed planar area of the protruding spheres. The bed was imaged every 40 s from above with two Prosilica GE 1650 cameras with a resolution of 1600 × 1200 pixels, equipped with Sigma 24 mm f1.8 EX DG macro lenses. The cameras were installed at a height of 2.10 m above the bed and perpendicularly to the bottom of the flume (Figure 1a). At each measurement location, the images yielded a 40 cm long and 30 cm wide (channel-width) field of view of the bed with a resolution of 17.14 px/cm. Since the Froude number was well below 1 for all experiments, surface perturbations were negligible and recordings through the water surface were possible.

The protruding spheres were identified in the images as uniform whitish regions with the lowest standard deviation in intensity levels as compared to the surrounding plastic granulate bed characterized by black and white patterns. On the basis of the planar area of a protruding sphere S_p, two parameters were computed for each sphere: the planar density λ_p and the mean level of protrusion $P = k/R$. λ_p is given by the ratio of S_p over half the reference-pattern's area $S_r/2 = l_x l_y/2$. P was determined on the basis of the equivalent radius $r_{eq} = \sqrt{S_p/(4\pi)}$ as follows:

$$P = \frac{k}{R} = \frac{R - \sqrt{R^2 - r_{eq}^2}}{R}. \tag{1}$$

Note that $P = 0$ and $\lambda_p = 0$ when the spheres are covered and reach maximum values of 1 and of 0.53, respectively, when the mean protrusion k reaches R, corresponding to the limit of the measurements. Since the error ϵ_P in determining P increases for k close to 0 and R, P was measured with a point gauge in the stoss and lee sides of a sample of five spheres for different bed levels and compared with the image-based protrusion for the same sample. The resulting ϵ_P/P is shown in Figure 2b. To estimate the error as P approaches zero where measurements are not feasible, a curve fit of the relative error based on the theoretical relationship $\epsilon_P = \epsilon_{r_{eq}} r_{eq} / \left(\sqrt{R^2 - r_{eq}^2}\right)$ is also shown (red line). An error of 0.02 cm for the equivalent radius, $\epsilon_{r_{eq}}$, was obtained from the best fit. It can be seen in Figure 2b that for $P > 0.05$ and $P < 0.8$, the relative error is less than 10%. These values were taken as cutoff for the applicability of Equation 1. The corresponding cutoff limits for the planar density were equal to $\lambda_p = 0.05$ and $\lambda_p = 0.51$.

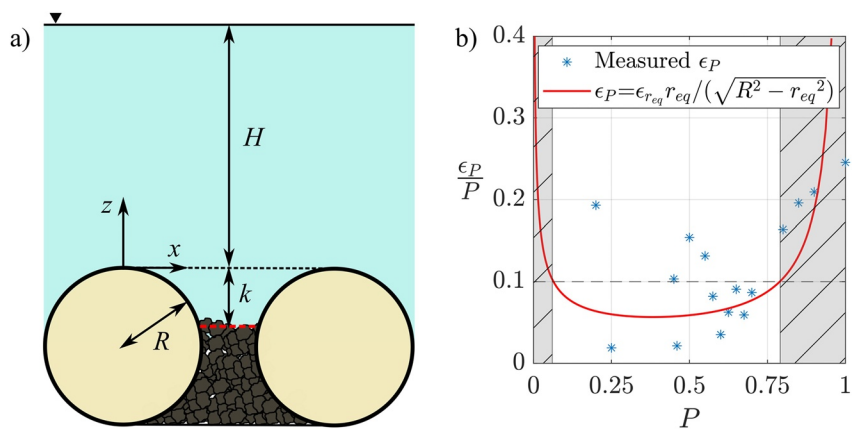

Figure 2. (a) Longitudinal view of two spheres on the bottom of the channel partially covered by sediments whose level defines the protrusion height of the spheres k and the normalized protrusion $P = k/R$; (b) Mean relative protrusion error ϵ_P/P as a function of P; the gray regions highlight the protrusion levels, which cannot be measured accurately as the relative error is higher than 10%.

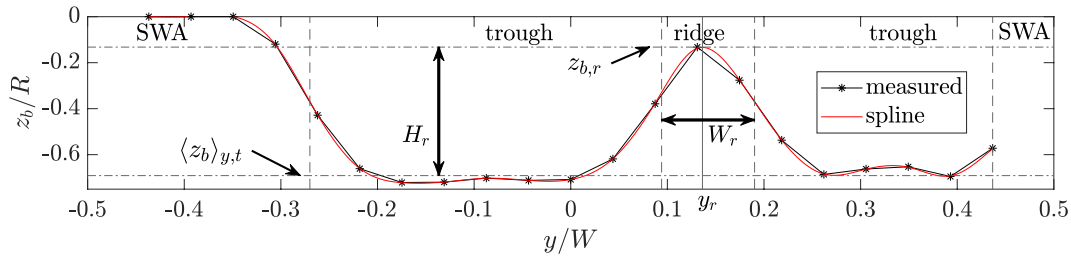

Figure 3. Transverse profile of the longitudinally-averaged bed elevations z_b for Exp. 1a (upstream), subdivided in troughs, ridge and side-wall accumulation (SWA) regions on the basis of the inflection points identified by the vertical dashed lines. y_r is the position of the ridge crest, $H_r = z_{b,r} - \langle z_b \rangle_{y,t}$ the ridge height and W_r the ridge width.

Since the main bedforms developing on the bed were longitudinal ribbons with ridges, troughs and side-wall accumulations, the topographic data were line-averaged in the longitudinal direction along the total field of view, i.e., 40 cm, so that for each timestep, transverse-protrusion $P(t, y)$ and planar-density $\lambda_p(t, y)$ profiles were obtained. To characterize the ridge morphology, the lateral position of the crest, height, width and side-slopes of the ridges were determined as follows: first, the transverse profiles of the longitudinally-averaged bed elevations $z_b(t, y) = -P(t, y)R$ were interpolated at each time step with a smoothing spline to determine the position of the crest of the ridges (y_r) with sub-pattern precision (Figure 3). This also allowed its inflection points to be computed (vertical dashed lines in Figure 3). The ridge width W_r was defined as the distance between the position of the inflection points on both sides of the ridge. The ridge height H_r was defined as the difference between the bed level at the crest $z_{b,r}$ and the bed level averaged in the troughs to the left and to the right of the ridge $\langle z_b \rangle_{y,t}$. The average slope of the ridge flanks s_r was determined as the mean value of the slope of the bed-level profile evaluated at the inflection points on the sides of the ridge. A ridge was considered significant if its height was larger than two times the standard deviation of the troughs' bed-level variation, which represents a robust statistical measure of the roughness height (Coleman et al., 2011). The side-wall accumulation's region was defined as the region comprised between the side-wall and the nearest inflection point of the bed to the side-wall (e.g., at $y/W \approx -0.27$ in Figure 3). If no inflection point was present in the vicinity of the wall, the inner edge of the side-wall accumulation was considered to be the first protruding sphere near the side-wall (e.g., at $y/W \approx 0.44$ in Figure 3).

2.4.2. PIV Measurements

The PIV measurements were performed in streamwise-oriented vertical planes, yielding the vertical and streamwise velocity components. To account for the variability of the flow in the spanwise direction, the measurements were performed both in the middle plane of the channel (m) at $y/W = 0$ and in the quarter plane (q) at $y/W = -0.22$, as shown in Figure 1d.

A 2W blue diode continuous laser was used to generate the laser sheet. The laser beam was expanded through a cylindrical diverging lens to a sheet with a thickness of 3 mm in the spanwise direction and a width of 10 cm in streamwise direction. Since the PIV system was based on a continuous laser, a high frequency camera was used to attain small enough time intervals for PIV correlations of images pairs. The camera, UI-3060CP-M-GL Rev.2 iDS with a resolution of 1936 × 1216 pixel and equipped with an AF DC-Nikkor 105 mm f/2 D lens, was installed perpendicularly to the laser sheet at a distance of 3 m from the flume glass wall (Figure 1d). The field of view spanned over one pattern of spheres from crest to crest, i.e., one l_x wide, and covered the entire water depth from the top of the spheres to the water surface (Figure 1a). Due to the presence of the spheres it was not possible to resolve the flow in the canopy region of the spheres. The flow was seeded with 10 μm micro-glass spheres.

A total of three PIV runs were performed at three different times during Exp. 1b and Exp. 5b in order to capture the flow at different erosive stages of the bed. For each of these runs at t = [21.2, 45.3, 69.3] h for Exp. 1b and t = [4.8, 18.6, 42.9] h for Exp. 5b, the flow field was acquired both in the middle and in the quarter plane. During each PIV measurement in one plane, 1,000 bursts were recorded at a burst frequency of 1.1 Hz, a time interval high enough to obtain statistically independent samples. The duration of the measurements (15 min) was short enough for the bed and the flow to be considered stationary. The bursts were processed with the Davis-PIV software version 8.4.0 based on a multipass iterative PIV algorithm with universal outlier detection by Westerweel

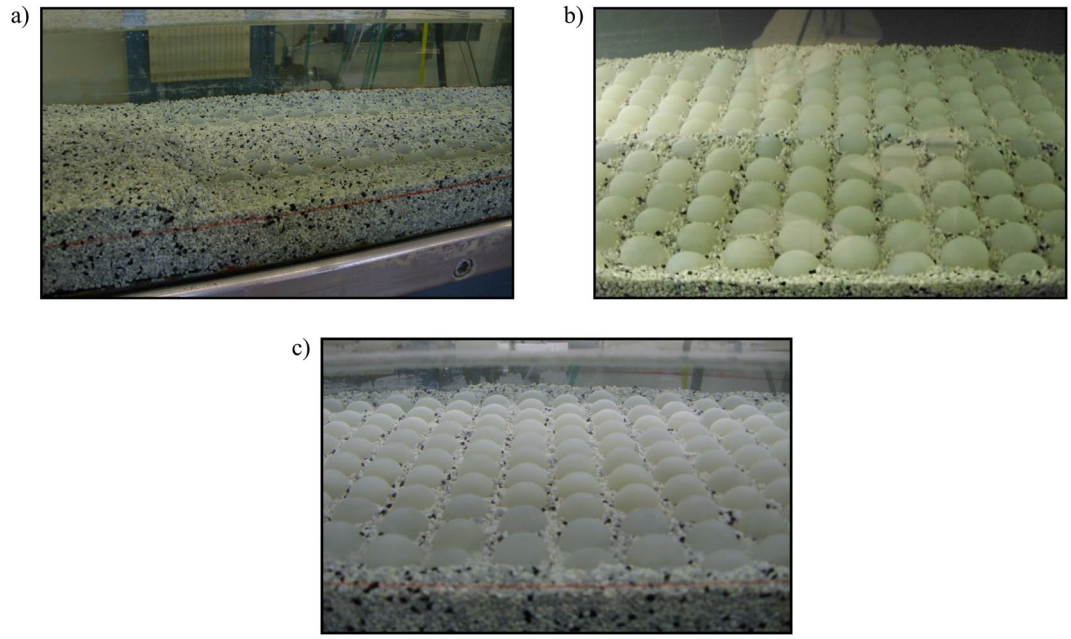

Figure 4. (a) Barchanoid dunes (on the left side of the picture) at $t = 0.5$ h during Exp. 5b with protruding spheres in the tail of the barchanoid downstream (not present in the picture). The flow is from left to right; (b) Longitudinal ridge in the middle of the flume at $t = 13$ h during Exp. 5b; (c) stable sediment bed reached at the end of Exp. 5b.

and Scarano (2005). The final correlation box size for all PIV measurements was equal to 12 × 12 pixels with a 50% overlap, resulting in a grid resolution of 1.1 × 1.1 mm^2.

Since the flow in the roughness sublayer is spatially heterogeneous, double averaging (Nikora et al., 2001) was performed in the longitudinal direction to determine the 1D profiles of the mean and turbulent flow statistics. Owing to the symmetry of the pattern, even though the measurements were performed only over its center (Figure 1b), this double averaging was equivalent to averaging three planes in the transverse direction.

3. Results

3.1. Global Description of the Bed Morphodynamics

At the beginning of the experiments, transverse bedforms, in the form of dunes or barchanoids, developed simultaneously along the entire length of the channel. Barchanoids are transitional bedforms between dunes and barchans with an almost crescent shape, as defined by Kleinhans et al. (2002). The development of dunes is expected for high sediment availability (Grams & Wilcock, 2007; Kleinhans et al., 2002; Tuijnder & Ribberink, 2009), which was given here by the initial sediment layer 1 cm thick over the spheres. In Exp. 1a/b (θlAm) and Exp. 4 (θlAh) with a low Shields parameter, clearly defined channel-spanning two-dimensional dunes were observed, gliding over a layer of non-moving fine sediments with no spheres appearing in the bed depressions in between the dunes' crests. The height of the dunes was equal or lower than the initial sediment layer thickness above the top of the spheres. Thus, it can be deduced that enough sediments were present on the bed to enable a full development of the dunes. However, in Exp. 2 (θmAm), Exp. 3 (θhAm) and Exp. 5a/b (θlAl) with medium and high shear or with medium and low aspect ratio, the bed was characterized by a sequence of barchanoids, spanning over half of the channel in checkerboard or pair-like patterns and characterized by the presence of regions of protruding spheres in their tail, as seen in Figure 4a. Thus, the entire initial sediment layer above the top of the spheres was mobilized in the barchanoids, possibly limiting the sediment availability for the full development of the bedforms. As shown by Tuijnder and Ribberink (2009), sediment-supply-limited conditions for the development of dunes (or barchanoids) over immobile gravel beds persist when the height of the dunes is larger than the average thickness of the sediments above the coarse immobile layer, as in the case just discussed. As in the present experiment, they also observed the presence of exposed regions of immobile gravel in between developing sand dunes with limited sediment supply.

The depletion of the first layer of sediments above the top of the spheres without upstream sediment feed led to the disappearance of the last traveling dunes after about 2 h in Exp. 2a/b (θmAm) and 1 h in Exp. 3 (θhAm) with medium and high shear stress, respectively, and after about 3.5–6 h in Exp. 1a/b (θlAm), Exp. 4 (θlAh), and Exp. 5a/b (θlAl) with low shear stress.

With the disappearance of the dunes and barchanoids, the spheres started to protrude permanently from the sediment bed. The evolution of the bed can now be quantified by determining how the longitudinally-averaged protrusion level $P(y, t)$ varies. $P(y, t)$ is plotted in Hovmöller (1949) diagrams shown in Figures 5a–5l. The diagrams are presented for both the upstream and downstream measurement locations, when available.

In all experiments shown in Figures 5a–5l, after an initial period with low protrusion levels ($P \leq 0.05$) when measurements are not possible, i.e., in the presence of the dunes, the bed development is characterized by increasing protrusion levels, implying that the sediments are being washed out. The bed is not eroded homogeneously though. For all experiments (Figures 5a–5l), the bed topography is characterized by high transverse heterogeneity due to the development of longitudinal low protrusion stripes, i.e., ridges, alternated with regions of higher sediment erosion, i.e., troughs. Side-wall accumulations with higher sediment levels are also present. A lateral pattern of smooth and coarse roughness stripes is created as shown in the physical image in Figure 4b for Exp. 5b with a ridge visible in the center of the channel.

It should be noted that the ridges do not develop abruptly. Indeed, they were already visually observed to form before the dunes disappeared. In Figure 4a, the two bed depressions in the tail of the barchanoids are, in fact, separated by a longitudinal sediment stripe, which continues to develop into a reach-spanning ridge after the dunes have disappeared.

Figures 5a–5l show that the ridges develop at different lateral positions. The beds of Exp. 1a/b, Exp. 2, and Exp. 3 are characterized by one asymmetric ridge developing on the left-hand side ($y > 0$). An asymmetry is also given by the presence of left and right side-wall deposits of different transverse extension, particularly evident in Exp. 1a and 1b (Figures 5a–5c). A single ridge develops also during Exp. 5a and 5b (Figures 5j–5l), but exactly in the middle of the channel leading to a symmetric bed topography. Both of these observations are reproducible, as can be seen by comparing Exp. 1a with Exp. 1b and Exp. 5a with Exp. 5b, which were run for the same flow conditions, respectively. Comparing the left (upstream) and the right (downstream) plots in Figure 5, the ridge evolution and positions do not change between the upstream and downstream measurement locations and can therefore be considered stable over the entire length of the flume. In Exp. 4, the development of two ridges is observed both at the upstream and downstream measurement location (Figures 5i and 5j), but at different times and different transverse locations. The reason for this discrepancy will be further investigated in Section 3.2.1.

From the bed evolution presented in Figures 5a–5l, it is apparent that the ridges persist for a longer time than the dunes in all experiments. Furthermore, the ridges erode more slowly than the troughs, the latter reaching P levels of about 0.7 in 1–2 h after the dunes. While the troughs continue to erode in Exp. 2 and Exp. 3, they reach a roughly constant level in all other experiments. In Exp. 1b, Exp. 4, and Exp. 5a (upstream), the ridges eventually flatten, establishing a uniform bed with no significant transverse variations in bed levels, as enough time is given to the system to develop. The same ridge flattening was visually observed in Exp. 2 and Exp. 3 for $P > 0.8$ when the measurements present high errors and then become impossible for $P > 1$.

In summary, two different bed behaviors are observed at the end of the experiments. In experiments with low θ (Exp. 1a/b, Exp. 4, and Exp. 5a/b), the bed reaches a stable condition with an almost constant and uniform protrusion level, consistent with visual observations of rare and sporadic movements of individual grains at the end of the experiments. Clearly, threshold conditions of motion have been reached due to grain sheltering induced by the spheres. In Exp. 2 (θmAm) and Exp. 3 (θhAm) with medium and high shear stress conditions, the bed is observed to erode completely to the glass plates. A final stable protrusion level is not reached, likely due to the fact that the grains can slide easily on glass when $P \simeq 2$ is approached. Nevertheless, it can be expected that a stable and uniform fine-sediment bed would be reached if the bed consisted of more levels of spheres filled with sediments.

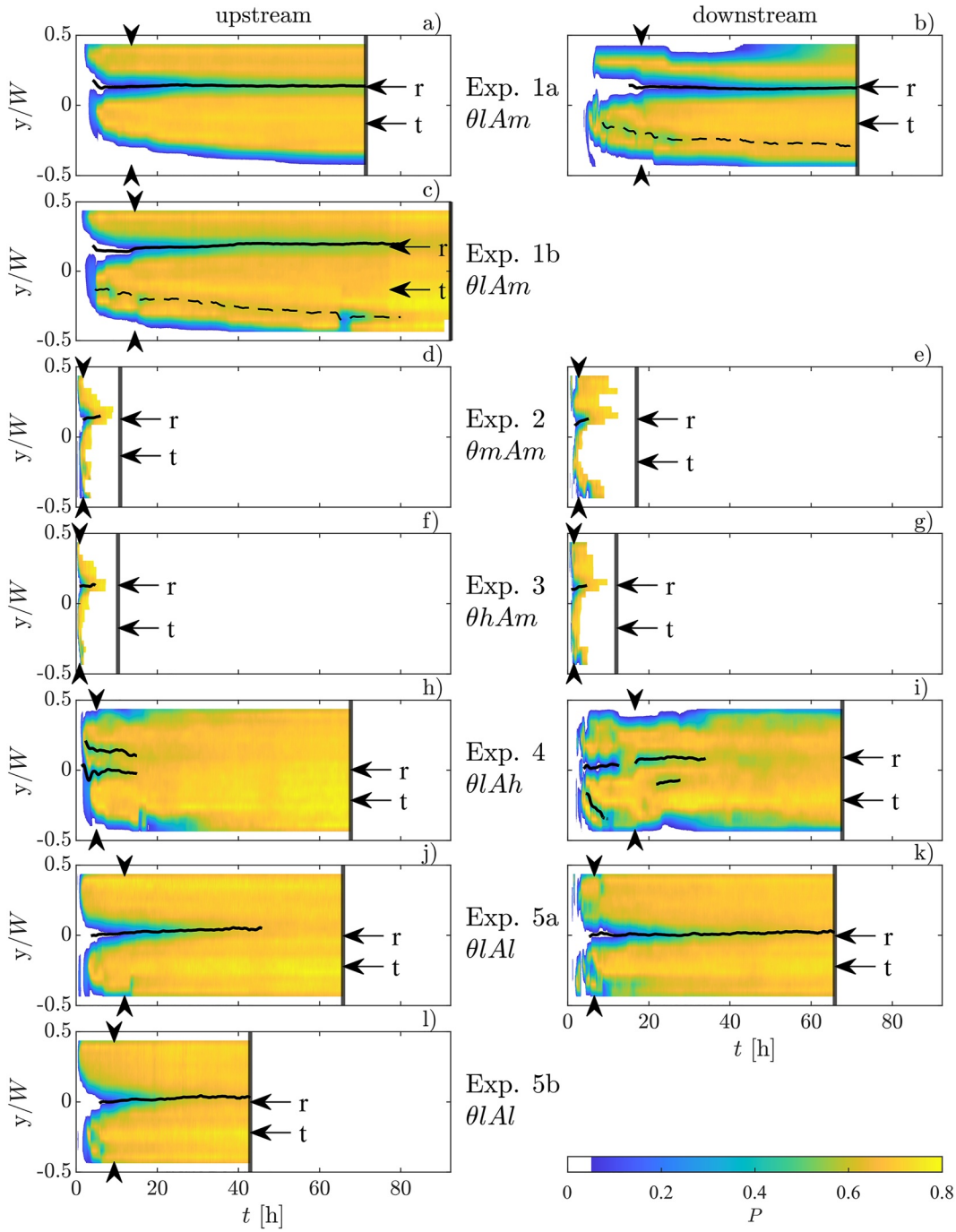

Figure 5. Hovmöller diagrams of the line-averaged protrusion P as a function of t and y/W; the continuous black lines identify the position of the peak of the ridges; the r- and t- arrows identify the ridges and troughs whose evolution is analyzed in Section 3.3; the vertical arrows identify the time for which the position and the width of the ridges have reached stationarity (see Section 3.2.2); the dashed lines in (b) and (c) identify secondary ridges; the vertical black lines identify the end of the experiments.

3.2. Ridge Morphology

3.2.1. Morphological Evolution

The morphological evolution of the observed ridges is analyzed on the basis of the morphological features defined in Section 2.4.1. In Figures 6a–6h, the temporal evolution of the normalized position y_r/W, height H_r/d_{50},

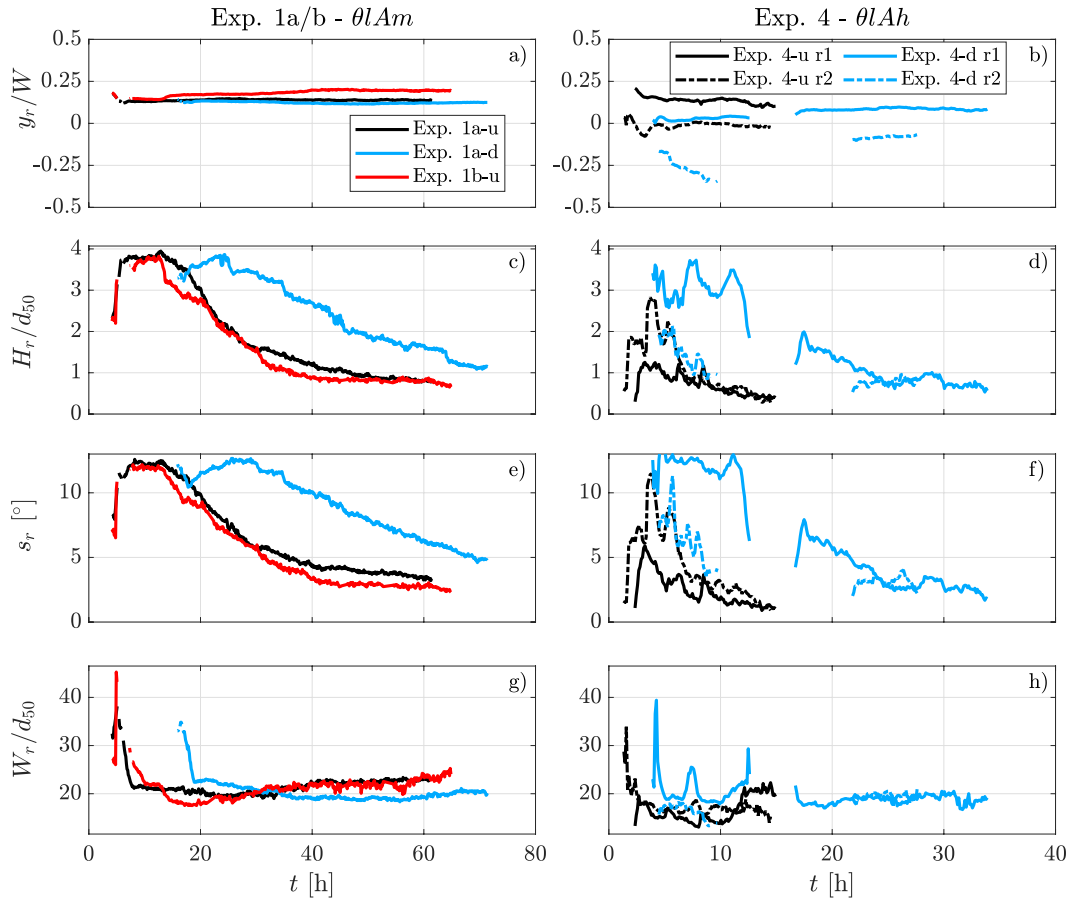

Figure 6. Normalized transverse position y_r/W, normalized height H_r/d_{50}, slope s_r and normalized width W_r/d_{50} of the ridges as a function of time. On the left column plots of Exp. 1a at the upstream (u) and downstream (d) measurement location and of Exp. 1b upstream; on the right column plots of Exp. 4 upstream and downstream with specification of the first ($r1$) and second ridge ($r2$).

width W_r/d_{50} and of the slope s_r of the ridges is presented for Exp. 1a/b (θlAm) and Exp. 4 (θlAh) at the up- and downstream locations. These experiments with medium and high aspect ratio were chosen to analyze the behavior of the bed in the presence of one and two ridges, respectively.

Figures 6a and 6b show that the transverse position of the ridges y_r/W is characterized by an initial phase of adjustment of 2–5 h, stabilizing then at an essentially constant transverse position. For Exp. 1a (Figure 6a), the positions of the ridge at the upstream and downstream measurement locations match very well. The position of the ridge of the repeated Exp. 1b (only measured upstream) is also very close. In Exp. 4, the ridges at the upstream measurement location (black profiles in Figure 6b) develop parallel to each other on the left side of the channel, whereas at the downstream location (blue profiles in Figure 6b), two pairs of ridges develop one after the other. The first pair of ridges at the downstream location develops during the first 10 h. It is characterized by a stable ridge in the center of the channel and a second ridge which drifts toward the right side of the channel, merging, in the end, with the side-wall accumulations. On the basis of the visual observation of the sequence of bed images, the central ridge disappears quickly at about 15 h, so that the development of the following pair of ridges at the downstream location is disconnected from the preceding one. The fact that the central ridge disappears and the second ridge drifts considerably to the side, shows that the first bed configuration is not stable. The second pair of downstream ridges, instead, produces a symmetric topographic pattern. The distance between these two ridges is similar to the distance between the ridges upstream (black profiles). This implies that the second ridge pair at the downstream location is, in fact, the pair of ridges first observed upstream, which have traveled downstream.

Figures 6c and 6d show that the normalized ridge height H_r/d_{50} increases rapidly, reaches a plateau and finally decreases. A similar trend also characterizes the evolution of the ridge slope s_r in Figures 6e and 6f. The plateaus

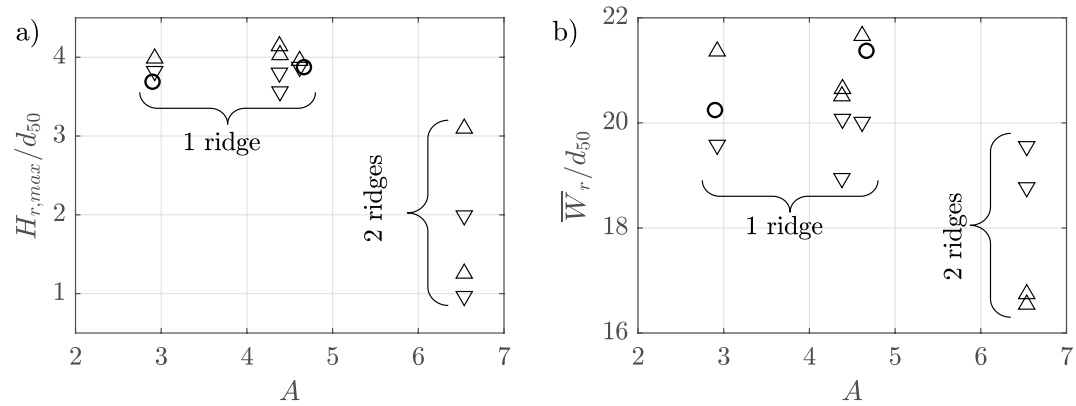

Figure 7. (a) Normalized maximum height of the ridges $H_{r,\max}/d_{50}$ and (b) normalized time-averaged width of the ridges $\overline{W}_r/d_{50}$ as a function of the aspect ratio A; (△) upstream location, (▽) downstream location and (○) upstream location in the repeated experiments.

reached by H_r/d_{50} and s_r suggest that the bed is eroding uniformly across ridges and troughs at this stage. The normalized ridge width W_r/d_{50}, in contrast, decreases during the initial growth phase of the ridge, quickly reaching a constant value (Figures 6g and 6h). The ridge obtains in this manner a triangular cross-section.

In Figures 7a and 7b, the normalized maximum ridge height $H_{r,\max}/d_{50}$ and the normalized time-averaged ridge width $\overline{W}_r/d_{50}$ are plotted as a function of the aspect ratio for all experiments (the time-average is computed when the width reaches a stable value after the initial rapid decrease, see Figures 6g and 6h). Figure 7b shows that all ridge widths are relatively close, between 16 and 22 d_{50}, although the ridge-pairs' widths at higher aspect ratio are generally lower. The normalized heights (Figure 7a) vary much more though. While for experiments presenting only one ridge, the maximum height is close to $4d_{50}$ for both aspect ratios ($A = [3, 4.5]$), $H_{r,\max}$ is comprised between 1 and 3 d_{50} for $A = 6.5$ with two ridges. Since the ridges develop when the initial sediment layer on top of the spheres is almost depleted, the lower maximum ridge heights detected in the case of pairs of ridges is likely related to the limited sediment availability partitioned in two instead of only one ridge. Since the single and the pair of ridges are characterized by almost the same width and the cumulative height of the pair of ridges is approximately equal to the height of a single ridge, the total sediment volume is about the same for the single and the pair of ridges. The ridges' height thus depends on their number, i.e., their spacing.

3.2.2. Lateral Spacing

The ridge spacing is defined at the time t_s for which the position and the width of the ridges do not significantly evolve anymore. In particular, t_s is defined as the earliest time instant for which the ridge position at all later times does not exceed one standard deviation around the globally time-averaged ridge position (the vertical arrows in Figures 5a–5l identify t_s). In the case of one ridge, the left- and right-wall ridge spacings, Λ_l and Λ_r, are defined as the distance between the position of the ridge and the inner edges of the side-wall accumulations, as shown in Figure 8a. In the presence of two ridges, a central ridge spacing Λ_c is included (Figure 8b). The effective width of the channel W_e is consequently defined as the distance between the inner edges of the side-wall accumulations (Figures 8a and 8b). It yields the effective aspect ratio $A_e = W_e/\langle H_e\rangle_y$, where $\langle H_e\rangle_y$ is the effective water depth averaged along the effective width W_e at time t_s with $H_e(y, t_s) = H + \langle\phi\,[k\,(x, y, t_s)]\,k\,(x, y, t_s)\rangle_x$. The effective water depth H_e accounts for the volumetric displacement induced by the spheres with ϕ the porosity of the bed given by $\phi = \int_{-k}^{0}\left[1 - \lambda_p(z)\right]dz$ and $\lambda_p = 2S_p(z)/S_r$ the planar density of a protruding sphere, as in Akutina et al. (2019). The ridge spacings Λ_l, Λ_r and Λ_c, all normalized by the effective water depth $\langle H_e\rangle_y$, are shown in Figures 8c and 8d for the upstream and downstream measurement locations, respectively. Since two consecutive ridge pairs develop during Exp. 4 at the downstream location, only the ridge spacings for the second ridge pair are plotted in Figure 8d.

Figures 8c and 8d (up- and downstream, respectively) show that for Exp. 5a and 5b (θlAl), characterized by one single ridge up- and downstream, both the left-wall and right-wall spacings are close to $1.3\langle H_e\rangle_y$. For Exp. 1a/b (θlAm), 2 (θmAm) and 3 (θhAm), also all with a single ridge, the left-wall spacings are close to $1.3\langle H_e\rangle_y$, while

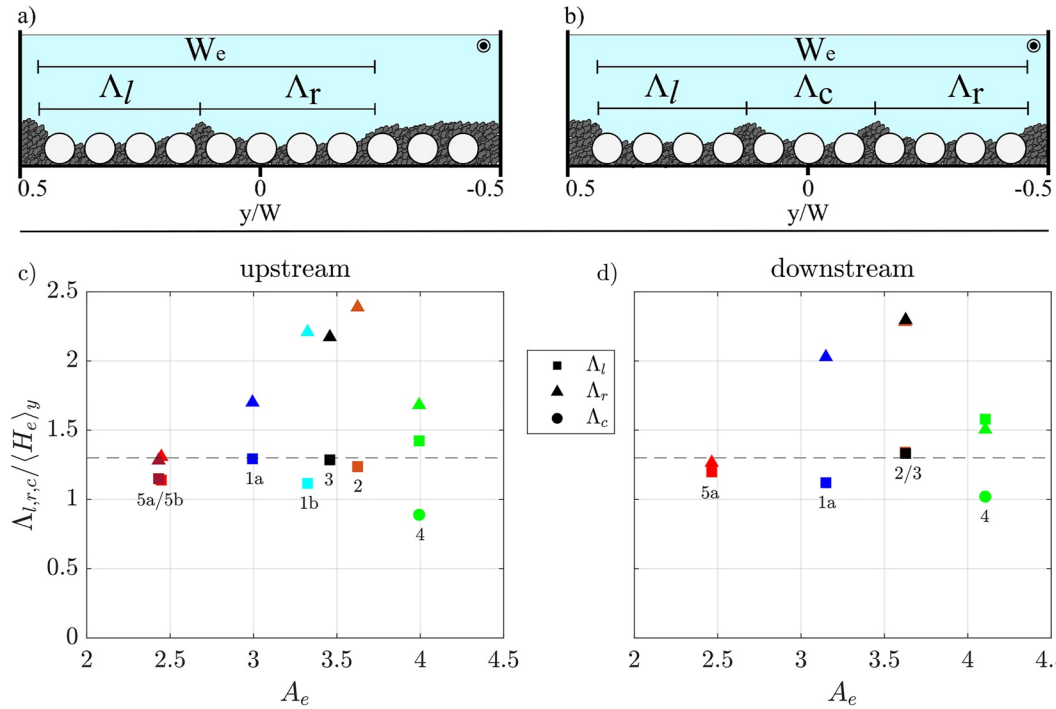

Figure 8. (a) Definition of the left-wall Λ_l and right-wall Λ_r spacings for one ridge (cross-sectional view); (b) definition of left-wall, right-wall and central spacings Λ_c for two ridges (cross-sectional view); (c, d) normalized left-, right-wall and central ridge spacings, $\Lambda_l/\langle H_e \rangle_y$, $\Lambda_r/\langle H_e \rangle_y$ and $\Lambda_c/\langle H_e \rangle_y$ as a function of the effective aspect ratio $A_e = W_e/\langle H_e \rangle_y$ for the upstream and downstream measurement location, respectively. The horizontal dashed line represents the theoretical ridge spacing derived by Colombini and Parker (1995).

the right-wall spacings vary between 1.7 and 2.4 $\langle H_e \rangle_y$. For Exp. 4 (θlAh), with two ridges, the left-wall and the right-wall spacings vary between 1.4 and 1.7 $\langle H_e \rangle_y$, while the spacing between ridges Λ_c is about $1\langle H_e \rangle_y$. In previous studies on longitudinal ridges in natural rivers or laboratory flumes with both uniform and bimodal sediment bed mixtures, the observed ridge-spacing to water-depth ratios were in the range of 1–3 in rivers (Culbertson, 1967; Karcz, 1966) and flumes (Ikeda, 1981; McLean, 1981; McLelland et al., 1999; Nezu et al., 1988; Wolman & Brush, 1961). Yet, Figures 8c and 8d suggest that the ridge spacing tends to be around $1.3\langle H_e \rangle_y$, ignoring the right-wall outliers for the moment. This spacing would agree with the linear stability analysis of an infinitely large river bed with bimodal sediments by Colombini and Parker (1995), who found a wavelength of $1.3H$ ($\equiv \Lambda_{Col}$) for maximum amplification of the system as a result of the interaction with the secondary currents in the absence of immobile roughness elements, where H is the water depth.

Taking Λ_{Col} as the characteristic ridge wavelength (provided that the effective water depth $\langle H_e \rangle_y$ is used in the presence of protruding roughness elements), provides a way to predict the number of ridges developing on the bed. When an integer number of Λ_{Col} -wavelengths fit into the effective width of the channel, then the number of ridges $N_r = N_\Lambda - 1$ where $N_\Lambda = W_e/\Lambda_{Col}$ ($= A_e/1.3$). In Table 4, the effective water depth $\langle H_e \rangle_y$, the effective width W_e, the effective aspect ratio A_e, the number of wavelengths N_Λ, the number of expected ridges $N_{r,e}$ and the number of observed ridges $N_{r,o}$ are listed. As can be seen for Exp. 5a/b for which N_Λ does not differ more than 0.1 from the nearest integer, $N_{r,e}$ corresponds to the number of observed ridges $N_{r,o}$ with the lateral wavelengths corresponding to Λ_{Col} (Figures 8a and 8b). Yet, even if an integer number of Λ_{Col} fit into W_e (within a tolerance of ± 0.1 to the nearest integer), it is also observed that the wavelengths can be higher or lower than the characteristic wavelength as seen in Exp. 4 (Figures 8a and 8b). The sum of the wavelengths, however, is equal to the effective width as can be deduced comparing the wavelengths for Exp. 4 in Figures 8a and 8b with W_e in Table 4.

Now, what happens if only a non-integer number of Λ_{Col} wavelengths fit into W_e with a fractional part within the range (0.1, 0.9)? In the case of Exp. 1a/b, Exp. 2, and Exp. 3, W_e does not correspond to an integer number of Λ_{Col}-wavelengths (Table 4). The number of ridges corresponds to the integer part of $N_\Lambda - 1$, as the good agreement between $N_{r,e}$ and $N_{r,o}$ for Exp. 1a/b, Exp. 2, and Exp. 3 in Table 4 shows. Yet, if the fractional part is higher

Table 4
Parameters for the Definition of the Number of Ridges

	1a		1b	2		3		4		5a		5b
Exp.	u	d	u	u	d	u	d	u	d	u	d	u
$\langle H_e \rangle_y$ (cm)	6.9	6.9	6.8	7.2	7.2	7.2	7.2	5.0	5.0	10.7	10.6	10.8
W_e (cm)	20.7	21.9	22.7	26.2	26.2	24.9	26.2	20.1	20.7	26.2	26.2	26.2
A_e (–)	3.0	3.2	3.3	3.6	3.6	3.5	3.6	4.0	4.1	2.4	2.5	2.4
N_Λ (–)	2.3	2.5	2.6	2.8	2.8	2.7	2.8	3.1	3.1	1.9	1.9	1.9
$N_{r,e}$ (–)	1	1	1	1	1	1	1	2	2	1	1	1
$N_{r,o}$ (–)	1	1	1	1	1	1	1	2	2	1	1	1

Note. Effective water depth $\langle H_e \rangle_y$, effective width W_e, effective aspect ratio A_e, number of wavelengths fitting in the effective width $N_\Lambda = A_e/1.3$, number of *expected* ridges $N_{r,e} = \text{int}(A_e/1.3 - 1)$, and number of *observed* ridges $N_{r,o}$ for all experiments both at the upstream and downstream measurement location.

than 0.5 and lower than 0.9, an additional ridge can develop as observed for Exp. 1a downstream and Exp. 1b upstream in Figures 5b and 5c (identified by the dashed lines). However, this additional ridge, which develops with a distance of Λ_{Col} from the primary ridge at time t_s, is very shallow, unstable and drifts toward the side-wall accumulation, eventually disappearing. We therefore do not count these in the number of observed ridges $N_{r,o}$ in Table 4. Thus, whenever there is a fractional part of $N_\Lambda \in (0.1, 0.9)$, lateral wavelengths wider than Λ_{Col} develop, as can be observed for the right-wall spacings Λ_r in Exp. 1a/b, Exp. 2, and Exp. 3 in Figures 8a and 8b.

The good agreement between $N_{r,e}$ and $N_{r,o}$ in Table 4 suggests that in addition to Λ_{Col} being the natural wavelength, the lateral side-wall accumulations, defining the effective width of the channel, adequately help to determine the number of ridges which develop. Since preferential upflow is expected to take place over the up-sloping inner edge of the side-wall accumulations, these act as virtual walls laterally bounding the development of the secondary currents' cells responsible for the ridges formation.

3.3. Evolution of the Ridge and Trough Protrusion Levels

In this section, the temporal evolution of the protrusion level P over the ridges and troughs is analyzed. The positions of the ridges and the troughs to be analyzed are identified through horizontal arrows in Figure 5 for all experiments. Figure 9 shows in black an example of the measured evolution of P for a single sphere in the trough in Exp. 5b (only the first 15 h are shown). Two main features can be noted. First, a time t_0 can be defined after which P remains positive, i.e., the sphere is not re-covered anymore. It can be noted that $t_0(x, y)$ is a function of the longitudinal and transverse position of the spheres within the measurement area, increasing in the longitudinal

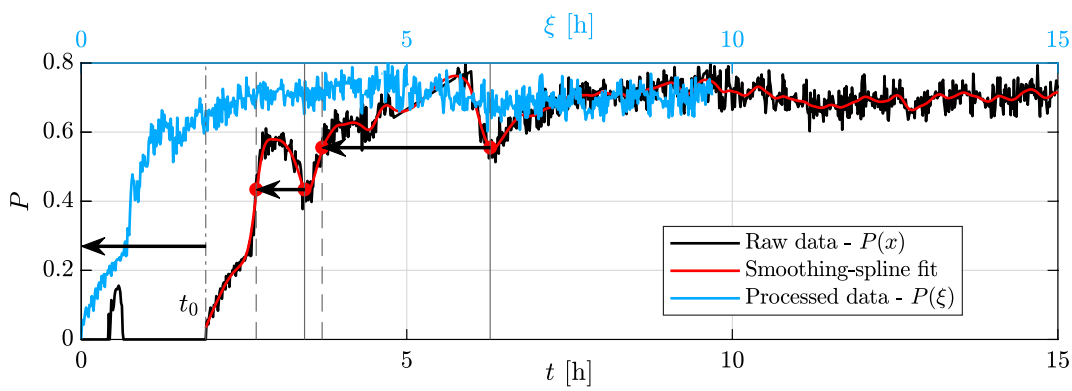

Figure 9. Example of data treatment of the temporal evolution of the protrusion levels of a sphere at the position of the trough during Exp. 5b for $t < 15$ h. In blue the raw signal (in red the interpolation via a smoothing spline) and in green the processed data obtained by: (a) shifting the raw signal by t_0, i.e., the time instant, when the spheres start to protrude, and (b) removing local maxima to where the protrusion level returns to its earlier level, to obtain a monotonic and comparable profile.

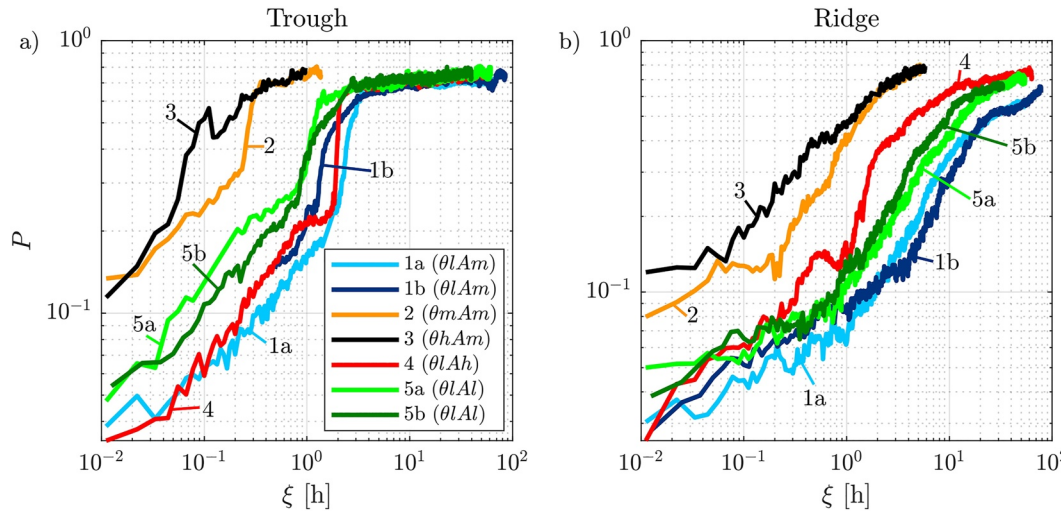

Figure 10. Line-averaged protrusion levels P as a function of $\xi = t' - t_0$: (a) trough, (b) ridge, at y-positions indicated with horizontal arrows in Figure 5 at the upstream measurement location for all experiments.

direction due to the advection of bedforms and displaying higher values over the ridges than over the troughs. Second, for $t > t_0$, the protrusion profile displays periods of local decrease in P, i.e., deposition, likely due to the appearance of sediment sheets traveling under the top of the spheres, temporarily causing increased bed levels. These depositional periods are identified in about 2% of the ridges' and troughs' profiles analyzed, while in all other profiles a purely monotonic increase of the protrusion levels is observed (with small-scale fluctuations falling within the measurement precision, see Figure 2b). Moreover, the depositional periods evidently do not modify the erosive behavior of the bed, as the variation of P in time is similar before and after the depositional pattern. Therefore, in order to effectively compare the different profiles and analyze only the erosive behavior of the bed, the P-signals are offset by t_0 and the depositional periods are removed. The new time frame $\xi = t' - t_0$ is defined, where t' is the time with the removed depositional patterns. These are defined between a local minimum and the point with the same protrusion level as the local minimum before the preceding local maximum (Figure 9). To this end, the protrusion profile is interpolated with a smoothing spline (red profile in Figure 9). The blue profile in Figure 9 illustrates the result as a function of ξ. Once the raw data are processed, the local protrusion levels $P(\xi, x)$ on the ridges and on the troughs are spatially averaged in the longitudinal direction (over nine spheres contained in the ridge's or trough's row of spheres within the 40 cm long measurement region) at each time step and denoted by $P(\xi)$.

Figures 10a and 10b show the temporal evolution of the longitudinally-averaged protrusion levels $P(\xi)$ at the upstream measurement location over the troughs and the ridges, respectively. The temporal evolution of P at the downstream measurement location is very similar and is not displayed. It can be seen that Exp. 2 and Exp. 3, which are characterized by medium and high θ, respectively, display the fastest evolution in protrusion levels for both the trough and the ridge positions, while Exp. 1a/b, Exp. 4, and Exp. 5a/b with low θ, evolve slower, as might be expected. Within the fast-evolving group, Exp. 2 (θmAm) evolves faster than Exp. 3 (θhAm), though. It should be noted that, as seen in Figures 5d–5g for Exp. 2 and Exp. 3, the bed erodes beyond $P = 0.8$, i.e., beyond the measurement range, so that only the initial bed development is displayed.

Over the troughs (Figure 10a), the protrusion levels of the spheres increase quickly from $P = 0$ to $P = 0.7$ within the first 0.5–3 h. Thereafter, a strong reduction in the evolution of the bed is observed, which eventually stabilizes somewhere in the range $0.75 < P < 0.8$. While Exp. 2 and Exp. 3 suggest a trend for further erosion of the bed (confirmed by the ultimate complete erosion of the bed, as observed visually), Exp. 1a/b, Exp. 4, and Exp. 5a/b reach an almost constant bed level associated with visually observed sporadic movement of individual grains.

Over the ridges (Figure 10b), the spheres reach protrusion levels as high as in the troughs but with much delay: after an additional 3 h for Exp. 2 and Exp. 3 and after an additional 30–40 h for Exp. 1a/b, Exp. 4, and Exp. 5a/b. As for the troughs, there is a significant slowdown in the evolution of the bed for high protrusion levels. Yet, while

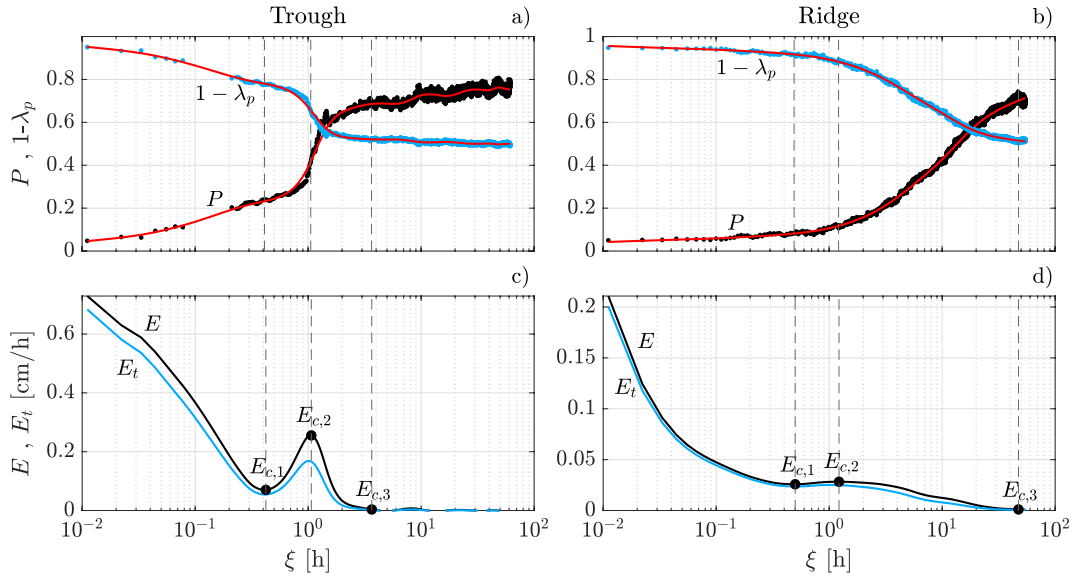

Figure 11. (a, b) Temporal evolution of the line-averaged protrusion levels P and of the surface area coverage $1-\lambda_p$ (the red lines are a smoothing-spline fit of the profiles); (c, d) Temporal evolution of the erosion rates $E = CR\partial_t P$ and of the total erosion rates $E_t = (1-\lambda_p)E$. The data are from Exp. 5a at the upstream measurement location. The left column are trough data while the right column ridge data. The dashed vertical lines represent the three transitions in erosive regime.

the troughs for Exp. 1a/b, Exp. 4, and Exp. 5a/b reach a quasi-plateau, the ridges do not reach quite such a stable bed level, even after 90 h in the case of the longest Exp. 1b.

The time rate of change of the protrusion level can be used to estimate the local erosion rate, which is related to the spatial variation in sediment transport rates in the presence of bedload through the Exner equation (Dey, 2014). The latter, however, was originally derived for uniform fine-sediment beds. Thus, a modified Exner equation is derived (Appendix A) to take into account the presence of immobile roughness elements by applying the conservation of mass of the mobile sediment fraction over a control volume defined over a pattern and excluding the roughness elements:

$$\frac{\partial q_s}{\partial x} = (1-\lambda_p)\,E = E_t \tag{2}$$

where E_t is the total erosion rate and $E = CR\partial_t P$ is the pattern-averaged erosion rate of a uniform bed in the absence of immobile roughness elements with $C = 1-\phi_s$ (=0.55) the fine sediment concentration (solidity). Compared to the original Exner equation, E is reduced by the longitudinally-averaged area coverage of the fine sediments $1-\lambda_p$. In order to calculate E_t, P (black dots in Figures 11a and 11b) and $1-\lambda_p$ (blue dots in Figures 11a and 11b) are fitted with a smoothing spline (red curves in Figures 11a and 11b). $\partial_t P$ is then estimated with a second-order central-finite-difference scheme.

Figures 11c and 11d show typical temporal evolutions of E_t and E over the troughs and ridges, respectively, for Exp. 5a upstream. First, it can be observed that E and E_t follow similar trends. The highest erosion rates, E or E_t, are observed just when the spheres start to protrude from the bed ($\xi = 0$), but are higher over the trough than over the ridge. The erosion rates then decrease non-monotonically, reaching an intermediate local maximum before eventually tending toward zero. As seen in Equation 2, E_t does not give a direct estimate of the sediment transport rate, but rather of the spatial variability in the sediment fluxes in the longitudinal direction. This implies that as long as E_t is positive, the bed is not in equilibrium as more grains are eroded than deposited in the measurement section. A state characterized by zero erosion rate, is either a consequence of equal sediment transport rates between upstream and downstream (resulting in a dynamic equilibrium) or a consequence of the cessation of sediment transport, i.e., $q_s = 0$ (resulting in a static equilibrium). Visual observations in the case of Exp. 1a/b, 4, and 5 show that, at the end of the experiments, the sediment transport is highly intermittent, i.e., close to zero, suggesting that the bed tends to a static equilibrium.

The local maxima in E_t and E reached at $\xi \simeq 1$ h both over the trough and the ridge in Figures 11c and 11d signify a temporary enhancement in erosion rates which is much more significant over the troughs than over the ridges. By comparing in Figures 11a and 11c and Figures 11b and 11d the contributions to the total erosion rates E_t which is a product of the area coverage $1 - \lambda_p$ and the erosion rates E, it is observed that the peak in the total erosion rates E_t derives from a steep increase in P, i.e., from E, while the area coverage only acts as a damper of the erosion rates E, as it monotonically decreases over time. In the following, the analysis of changes in erosive behavior is performed on the basis of the erosion rate E to avoid the small influence of the area coverage.

The temporal evolution just discussed can be separated into four different regimes, the transition points being marked by black dots in Figures 11c and 11d: the first regime is characterized by a fast and monotonic decrease in the erosion rate, the second by a growing erosion rate, the third by a decrease again and the fourth by a negligible erosion rate. The critical protrusion levels, labeled P_{ci} with $i = 1, 2, 3$, corresponding to the three marked transitions are defined at the times ξ when the erosion rates E reach the local minimum (E_{c1}), the local maximum (E_{c2}) and 0.5% of the erosion rate E_0 at time $\xi = 0$ (E_{c3}). These three critical levels P_{ci} are plotted as a function of the Shields parameter in Figures 12a and 12b for the troughs and ridges, respectively. P_{c1}, P_{c2}, and P_{c3} are connected by continuous, dashed and dot-dashed lines, respectively. For the troughs, Figure 12a shows that the three critical protrusion levels do not depend on the Shields parameter θ, since each critical point takes place at almost the same protrusion levels for all experiments: $P_{c1} \simeq 0.2$, $P_{c2} \simeq 0.4$, and $P_{c3} \simeq 0.7$. A dependency on the aspect ratio A is also excluded, as the experiments are characterized by different A. It should be noted that in the case of Exp. 2 downstream and Exp. 3, the first two transitions are not observed, since the measurements are probably not time-resolved enough to capture them. In the case of the ridges, Figure 12b shows that the first two transitions take place for lower protrusion levels compared to the troughs (Figure 12a) and are not quiet as constant. The first transition is observed for $P_{c1} \simeq 0.1$–0.2 and the second transition for $P_{c2} \simeq 0.2$–0.4. The third transition displays, instead, similar protrusion levels as over the trough ($P_{c3} \simeq 0.7$).

While the transitions in bed behavior take place at essentially the same bed level for all Shields parameters and aspect ratios, the time instants at which the transitions occur, defined as ξ_{ci}, decrease with increasing θ, as shown, for example, in Figures 12c and 12d for the time instant associated with the second transition ξ_{c2}. In Figures 12e and 12f, the erosion rates E_{c2} at the second transition show also a dependency on θ: the higher θ, the higher the peak erosion rates E_{c2}. A similar trend is also observed for E_{c1}, E_{c3}, and E_0 (not shown here). The relative increase in the local peak erosion rate, E_{c2}/E_{c1} shown in Figures 12g and 12h, shows that over the troughs, $E_{c2}/E_{c1} \simeq 2$–4.5, and over the ridges, $E_{c2}/E_{c1} \simeq 1$–2. The increase of the peak in erosion rates is evidently much less pronounced over the ridges than over the troughs. Among the different experiments, Exp. 4 shows higher E_{c2}/E_{c1} ratios both over the troughs and the ridges, possibly due to the higher aspect ratio corresponding to a lower relative submergence (ratio between the water depth and the protrusion level of the spheres). Compared to the erosion rate E_0 at $\xi = 0$ when the spheres start to protrude, Figure 12i shows that over the troughs $E_{c2}/E_0 \simeq 0.4$–1 for low θ, while for high θ it can be higher than one, a clear case of shear-stress enhancement. Over the ridges, Figure 12l shows that with increasing θ, E_{c2}/E_0 increases and can reach values as high as 1.

3.4. Flow Over Troughs and Ridges

3.4.1. Flow Profiles

The PIV measurements performed during Exp. 1b (θlAm) and Exp. 5b (θlAl) are analyzed to characterize the development of the secondary currents with simultaneous changes in bed topography and roughness resulting from the development of the ridges and the changes in the sphere's protrusion, respectively. Figures 13a and 13b display the temporal evolution of the protrusion levels P measured upstream of the PIV system at the same transverse location of the two PIV planes at $y/W = 0$ (m = middle plane) and at $y/W = -0.22$ (q = quarter plane). The vertical lines highlight the times t_1, t_2, t_3 around which the PIV measurements were performed. In Figures 13c and 13d, the transverse profile of P measured just ahead of each PIV run is displayed. Figure 13c shows that during Exp. 1b, the m- and q-planes are located over the trough region (maximum P values), which has reached a quasi-stable level for all three PIV measurements (Figure 13a). However, the ridge in Exp. 1b, situated at $y/W = 0.22$, is still evolving, as seen in Figures 13a and 13c. In Exp. 5b (Figures 13b and 13d), the PIV planes are located over the ridge in the m-plane and over the trough in the q-plane. The bed is still evolving in the m-plane (ridge), while it has reached a stable bed level in the q-plane (trough) at t_2 and t_3.

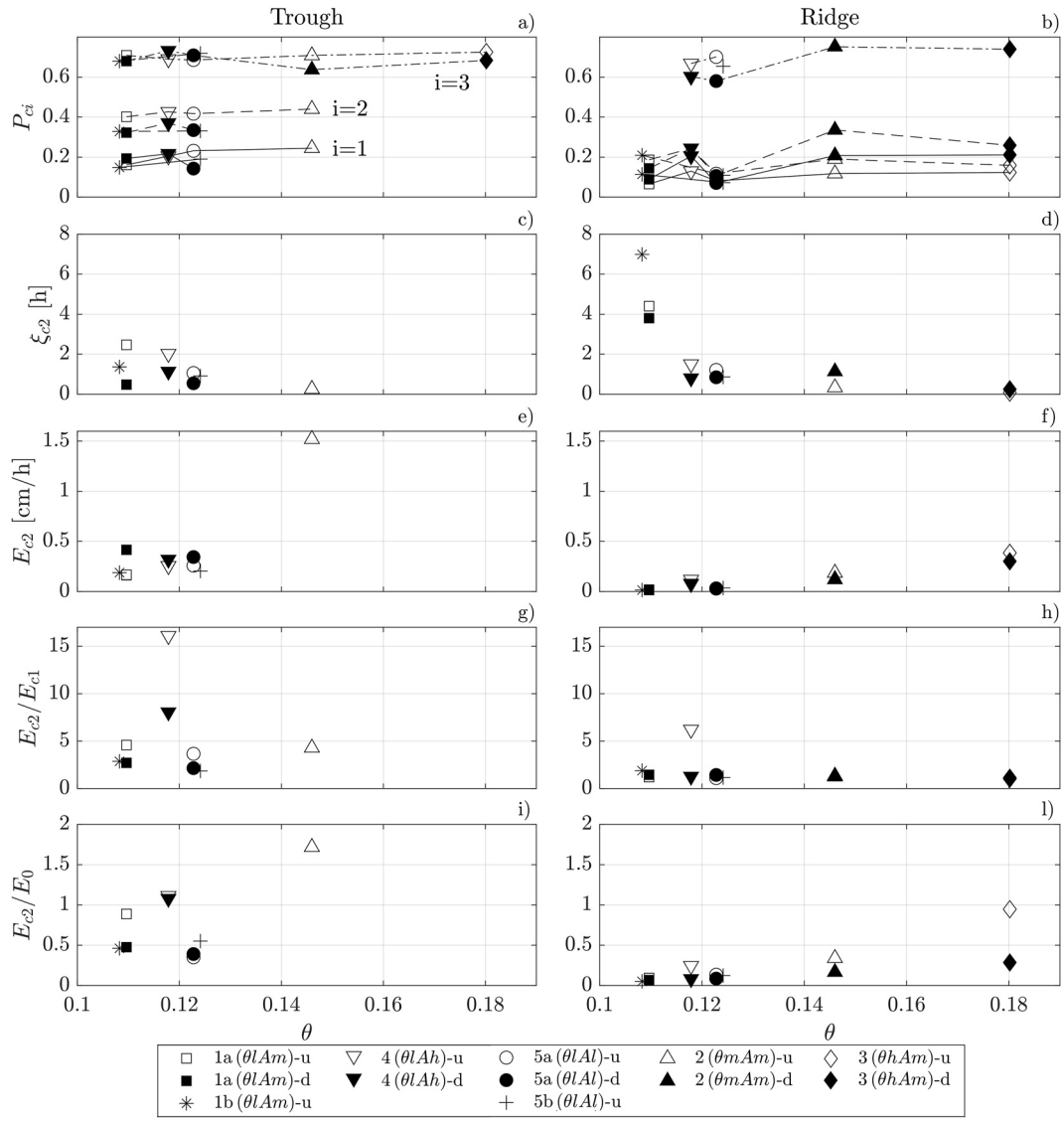

Figure 12. Critical values at the transitions in erosive regime as a function of the Shields parameter θ for the trough (left column) and the ridge (right column): (a, b) Critical protrusion levels P_{ci}; (c, d) critical time at the second transition ξ_{c2}; (e, f) erosion rate at the second transition E_{c2}; (g, h) ratio between E_{c2} and the erosion rate at the first transition E_{c1}; (i, l) ratio between E_{c2} and the erosion rate at $\xi = 0$, E_0. For diagrams (a) and (b), the continuous lines identify the critical points for the first transition, the dashed lines for the second transition and the dot-dashed lines for the third transition.

In Figures 14a–14f, the vertical profiles of the time- and longitudinally-averaged streamwise and vertical velocities, $\langle\overline{u}\rangle_x$ and $\langle\overline{w}\rangle_x$, as well as the longitudinally-averaged profiles of the Reynolds shear-stresses $-\rho_f\langle\overline{u'w'}\rangle_x$ are plotted (with $z/H = 0$ corresponding to the top of the spheres). The horizontal dashed lines in Figures 14b, 14d and 14f for Exp. 5b represent the fine-sediment bed level during the first PIV run in the m-plane which was higher than the top of the spheres. This level was extracted from the PIV images.

Figure 14b (Exp. 5b) shows that over the ridge (m-plane), the streamwise velocity profile reaches a maximum at the water surface, while over the trough (q-plane), the velocity profile is characterized by a velocity dip. This is consistent with the upflow and downflow taking place over the ridge and over the trough (Figure 14d), respectively, as the result of counter-rotating secondary currents (McLelland et al., 1999; Nezu & Nakagawa, 1984, 1989; Vanderwel & Ganapathisubramani, 2015). In Figure 14b, the vertical location of the velocity dip remains constant at about 70% of the water depth for all PIV runs, as the downflow over the trough does not change. On the other hand, the streamwise maximum velocity observed at the water surface over the ridge increases with time, since

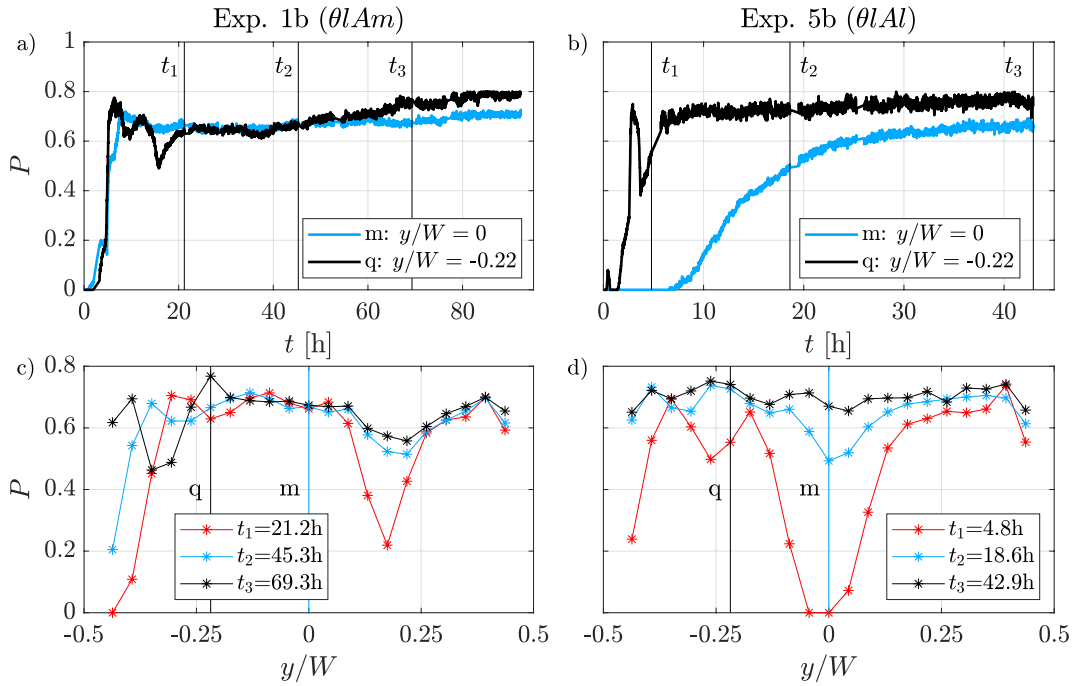

Figure 13. (a, b) Line-averaged protrusion-level profiles P as a function of time in the middle (m: $y/W = 0$) and quarter plane (q: $y/W = -0.22$) during Exp. 1b and 5b (the vertical lines identify the time instants at which the Particle Image Velocimetry (PIV) runs were performed); (c, d) Transverse profiles of the line-averaged protrusion level P just before the PIV runs for Exp. 1b and 5b (the vertical lines identify the PIV planes).

the upflow decreases (Figure 14d), i.e., the advection of low momentum budgets to the water surface being associated with it (Nezu & Nakagawa, 1984; Vanderwel et al., 2019; Willingham et al., 2014). The decrease of the upflow over the ridge is concomitant with a decrease in the ridge's height (Figure 13d), highlighting that the intensity of the secondary currents changes as the result of changes in the ridge morphology.

Figure 14d also reveals that the upflow over the ridge is stronger than the downflow over the trough. In agreement with this, the transverse bed topography profile (Figure 13d) shows that the trough width is wider than the ridge width, so that per continuity the downflow needs to be less strong than the upflow. While the downflow reaches a maximum value equal to 2% of the maximum streamwise velocity $\langle \overline{u} \rangle_{x,\max}$, the upflow reaches values three times as high ($\simeq$6%) at t_1. These upflow values are quite remarkable, as they usually do not exceed 3% $\langle \overline{u} \rangle_{x,\max}$ over ridges in weakly bimodal sediments (McLelland et al., 1999).

The signature of secondary currents can be also observed in the case of Exp. 1b. Figure 14a shows that the dip phenomenon takes place both in the m- and q-plane, consistent with downflow taking place in both planes positioned over the trough (Figure 14c). In the m-plane, the streamwise-velocity profiles increase over time at the water surface and decrease near the bed, since the downflow decreases (Figure 14c). Even though the bed level does not change over the trough (Figure 13c), the decrease in downflow is likely connected to the decreasing height of the ridge positioned at $y/W = 0.2$. The distance between the ridge and the m-plane, equal to $0.2W$, corresponds in fact to approximately half the characteristic interridge spacing of $1.3H_e$ found in Section 3.2.2, i.e., to the size of the secondary current cell influenced by the ridge.

The normalized Reynolds shear-stress profiles, shown in Figures 14e and 14f, are not linear as in uniform and steady 2D open-channel flows. In Exp. 5b (Figure 14f), the Reynolds shear-stress profile is convex in the q-plane where downflow takes place and concave where upflow takes place (Figure 14d), in accordance with previous studies on fixed ridges (Nezu & Nakagawa, 1984; Wang & Cheng, 2005). The peak shear stress is not observed at the level of the roughness crests, but is displaced upwards, a typical feature of shear stress profiles in the presence of secondary currents (McLelland et al., 1999; Nezu et al., 1988). Over the ridge, the upflow induces an upward shift of the shear stress peak up to 20% of the water depth, while over the trough the peak is pushed toward the roughness crests by the downflow. In Exp. 1b, the Reynolds-shear-stress profiles over the trough display typical

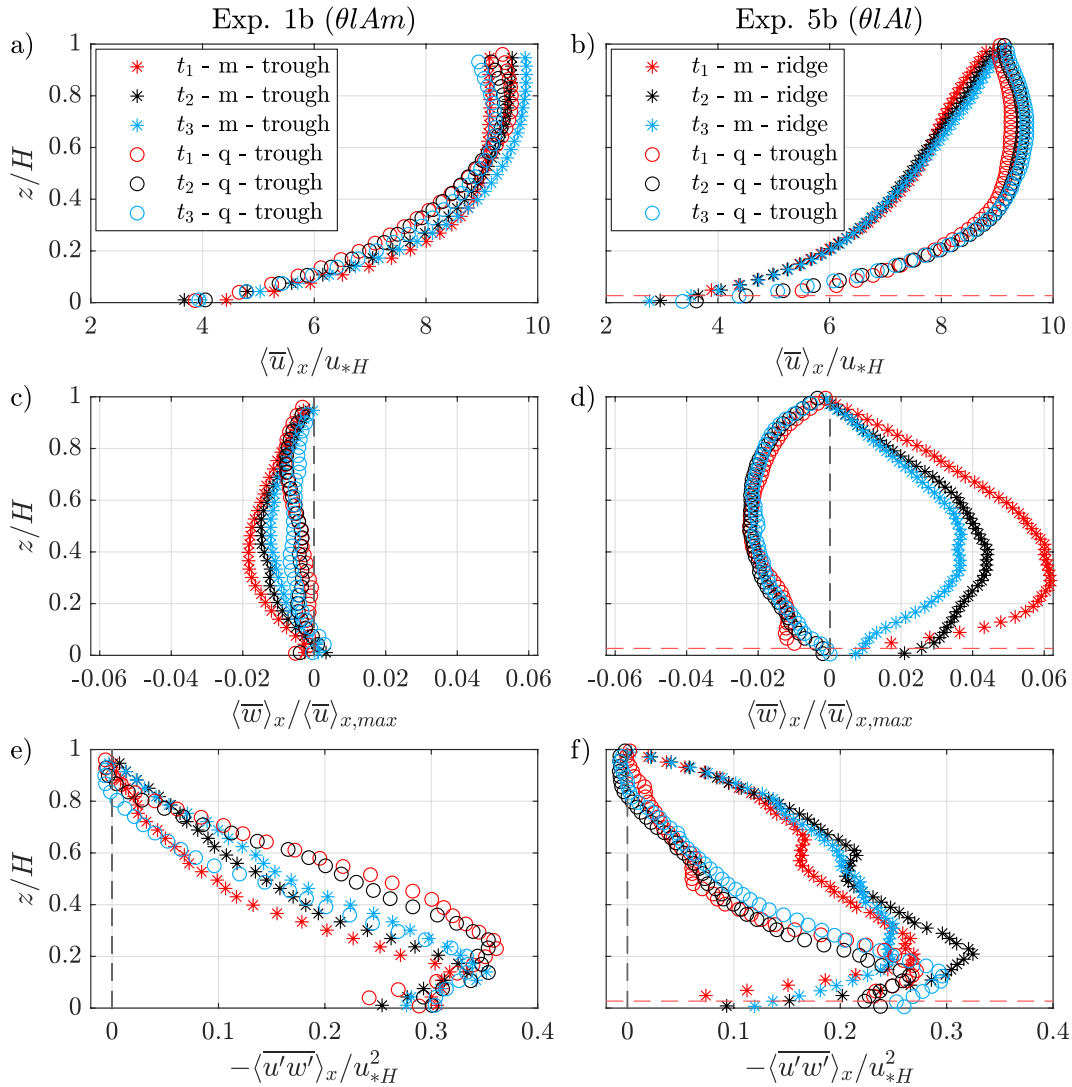

Figure 14. Vertical profiles of the normalized double-averaged streamwise velocity $\langle\overline{u}\rangle_x/u_{*H}$ (a, b) and vertical velocity $\langle\overline{w}\rangle_x/\langle\overline{u}\rangle_{x,\max}$ (c, d) and of the normalized longitudinally-averaged Reynolds shear stress $-\langle\overline{u'w'}\rangle_x/u^2_{*H}$ (e, f) for Exp. 1b and 5b for both the middle and the quarter plane. The dashed red line in the plots of Exp. 5b represents the fine-sediment bed level in the m-plane during the first PIV run.

convex shapes (Figure 14e) associated with the downflow. Accordingly, the convexity is more pronounced for the shear-stress profiles measured in the m-plane where the downflow is stronger (Figure 14c).

3.4.2. Shear Stress in the Near-Bed Region

Near the roughness elements for $0 < z/H \lesssim 0.1$, the Reynolds shear-stress is influenced by the bed roughness with, accordingly, higher turbulent shear stress values over the trough than over the ridge, as seen in Figure 14f for Exp. 5b during which the flow is measured both over the ridge and the trough. Since P is lower for a ridge than for a trough, the ridge is indeed smoother than a trough. The differences in shear stress between the ridge and the trough are also in good agreement with the higher erosion rates observed over the ridges than over the troughs in Section 3.3.

The local shear velocity $u_* = \sqrt{\tau_{xz}/\rho_f}$ acting at canopy top is determined on the basis of the total fluid shear stress τ_{xz}, i.e., the sum of the viscous, form-induced and Reynolds shear stress (e.g., Nikora et al., 2001), at the top of the spheres. Figures 15a and 15b show the evolution of the local shear velocity u_* normalized by the total shear velocity obtained from the water depth u_{*H} as a function of P in the m- and q-planes for Exp. 1b and Exp. 5b,

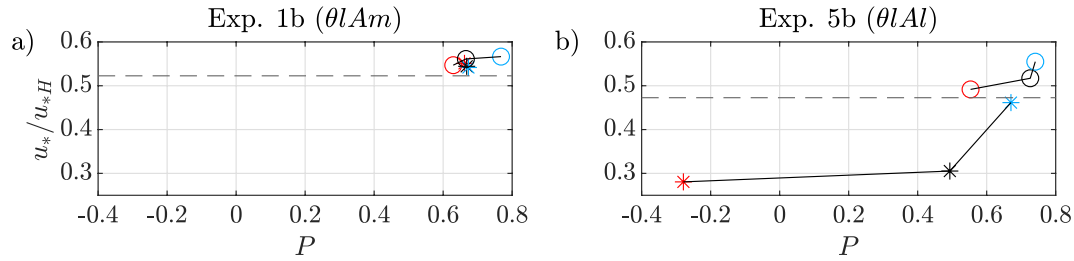

Figure 15. Local shear velocity acting at the top of the roughness u_* normalized by the total shear velocity obtained from the slope-depth product u_{*H} as a function of the local protrusion level P. The colors and symbols are equivalent to the ones used in Figure 14 (∗, m-plane; ○, q-plane). The horizontal dashed line represents the threshold of motion for permanent grain movement.

respectively. It can be observed that u_* is just 30%–50% of u_{*H}, which represents the total momentum exchanged by the flow at the canopy top. This reduction can be explained by considering that in the presence of secondary currents, the gravitational force is not only balanced by the total fluid shear stress, but also by the convective and the transverse shear stresses (Nezu & Nakagawa, 1993). As such, the total fluid shear stress measured at the canopy top in the presence of secondary currents does not match the total shear stress u_{*H}, as observed by Coleman et al. (2007) for secondary currents developing over transverse bars.

Figure 15b for Exp. 5b allows to compare the evolution of the shear velocity between troughs and ridges since they are captured by the q- and m- planes, respectively. It can be seen that u_*/u_{*H} increases slightly between t_1 (red star) and t_2 (black star) both over the ridge (m-plane) and the trough (q-plane), implying that the lateral roughness gradient remains essentially constant. Yet, in the same time interval, the protrusion level over the ridge increases significantly, i.e., the ridge height decreases. The reduction in the upflow over the ridge, observed in Figure 14d for these initial times between t_1 and t_2, can therefore be ascribed to a reduction in the height of the ridge (i.e., in its aspect ratio, since the ridge width is constant, see Section 3.2). For later times, however, there is a significant increase in u_*/u_{*H} over the ridge between t_2 and t_3 (black and blue stars in Figure 15b, respectively) associated with a relatively small increase in P, while over the trough, u_*/u_{*H} remains quasi constant. This implies that over the ridge, the lateral roughness gradient decreases significantly while the ridge height barely evolves. The reduction in upflow between t_2 (black star) and t_3 (blue star) seen in Figure 14d can therefore be ascribed to the decreased lateral roughness variability rather than the ridge height evolution as between t_1 and t_2. In summary, the analysis of the local shear velocities in comparison with the vertical velocities of the secondary currents, reveals that for low protrusion levels, the intensity of the secondary currents over the ridges is primarily influenced by variations in the ridge height, while for high protrusion levels, the intensity is primarily influenced by the decreasing lateral variations in roughness.

The expected normalized critical shear stress for the onset of motion given by the Shields diagram for uniform beds is also included in Figures 15a and 15b by a dashed line. For both experiments, it can be seen that the local shear stress above the troughs is above the threshold of motion for t_1, t_2, and t_3, even though the bed has reached a quasi-constant protrusion level (Figures 13a and 13b). This confirms the sheltering effect of the protruding spheres: as the spheres extract momentum from the flow, they reduce the shear stress acting on the fine sediments.

For the ridge in Exp. 5b (Figure 15b), on the other hand, at times t_1 and t_2 in particular, the total shear stress at the canopy top is below the threshold, i.e., no erosion would be expected. Yet, the ridge is eroding, as seen in Figure 13b. At t_1, P is negative over the ridge, i.e., the spheres are covered by grains, so that the measured shear stress acts directly on the fine sediment. Since in this case, there is no possible shear enhancement due to the absence of protruding spheres, the erosion is surmised to be due to strong turbulent events impacting the bed, whose contribution is averaged out in the time-averaging of the Reynolds shear stress. To pursue this conjecture, a quadrant analysis was performed (Appendix B) to quantify the sweep events which have been suggested to be responsible for sediment bed-transport (e.g., Hofland et al., 2005; Nelson et al., 1995; Sechet & Guennec, 1999). The results given in Appendix B show that near the bed, the intensity of the sweep events is slightly higher than the critical shear stress for permanent grain motion. This could explain the observed slow sediment transport over the ridges, at least for t_1 in Exp. 5b when the spheres are covered. The sweep events with the highest intensity, which dominate usually the near-bed region over uniform rough beds in the absence of secondary currents (Dey

& Das, 2012; Mignot et al., 2009), are displaced away from the fine-sediment bed by the dominant upflow over the ridges (Appendix B), which leaves the more quiescent sweeps near the bed. Nevertheless, these are still able to set the fine sediments in motion, while the total shear stress near the bed is reduced below the critical shear stress. Over the troughs, on the other hand, the downflow advects the sweeps with the highest intensity toward the bed (Appendix B), leading to higher erosion rates as compared to the ridges. Given that the fine sediments in the troughs for Exp. 5b at t_2 and t_3 are essentially not eroding anymore (Figure 13b), the strong sheltering effect of the protruding spheres is highlighted again, which evidently shelter the fine sediments from the sweep events with the highest intensity.

4. Discussion

4.1. Global Morphological Evolution

As the fine sediments erode below the spheres's top with a subsequent reduction of the area covered by fine sediments, a transition between three-dimensional reach-spanning dunes to two-dimensional ribbons is observed, as in previous studies on erosion for bimodal sediment mixtures (Kleinhans et al., 2002) and fine sediments over a rough bed (Grams & Wilcock, 2014; McLean, 1981). Here, it is observed that a smooth transition occurs during which the two bedforms overlap, with ribbon-like sediment structures developing in the tails of the dunes. Since the imposed bed shear stresses in the present experiments lead to Shields parameters (Table 1) which lie above the range for the appearance of ribbons for uniform sediments $\theta \in [1\theta_c, 3\theta_c]$ according to Hirano and Ohmoto (1988), the development and stabilization of ribbons when the spheres protrude can be attributed to the spheres' presence. However, before the bed erodes below the spheres' top, dunes are the dominant bedform at these Shields parameters, in agreement with Hirano and Ohmoto (1988). The presence of protruding immobile grains therefore allows sediment ribbons to stabilize for shear stress conditions for which dunes would otherwise have been the dominant bedform.

The ribbons shape the bed topography even when they lie below the spheres' top, until they disappear, yielding a stable and uniform bed level. This can be observed in Exp. 1b, Exp. 4, and Exp. 5b which were long enough to observe this (Figure 5). The troughs and ridges evolve differently, though. The troughs are quickly depleted of sediments and reach a stable bed level within a few hours owing to the higher sheltering effect of the spheres (higher protrusion levels). The ridges, instead, persist for days, becoming the main sediment source before eventually disappearing by reaching the same sediment level as the troughs. For the broader purpose of fine-sediment decolmation from a clogged gravel bed, this suggests that the presence of ridges locally slows down the process, but eventually the fine sediments are eroded to a uniform sediment bed within the bed interstices.

4.2. Ridge Morphodynamics

In the initial development phase, the ridges are observed to meander slightly in the transverse direction for a few hours before reaching a stable transverse position (Figures 6a and 6b), close to their initial position when they develop in the tail of dunes. Accordingly, the number of ridges remains stable thereafter. Scherer et al. (2022), on the other hand, found via their DNS study that the ridges meander and coalesce over time leading to a reduction of the total number of ridges before stabilizing. However, they considered an infinitely wide channel with a uniform fine-sediment bed. Scherer et al. (2022) associate this behavior to the meandering behavior of large-scale high- and low-velocity streaks which induce regions of high- and low shear stress. Here, the limited transverse meandering of the ridges is evidently associated with the lateral containment of the secondary currents due the presence of side-walls, which stabilizes the longitudinal regions of lower shear stress in the transverse direction.

The morphological evolution of the ridges in a rough immobile bed is characterized by an initial rapid increase of the ridge's height (Figures 6c and 6d) and side-slopes (Figures 6e and 6f) and by a decrease of the ridge's width (Figures 6g and 6h). These three morphological changes lead to an increased lateral roughness heterogeneity (see P levels, Figure 5) and to a triangular cross-section. The heterogeneity and triangular cross-section, in turn, along with the decrease in ridge width, are expected to lead to an increase in the intensity of the secondary currents as shown by studies on fixed artificial ribbons (Medjnoun et al., 2020; Wang & Cheng, 2006; Willingham et al., 2014). Thus, it is likely that a self-enhancing mechanism exists in which the increased secondary currents induce higher shear stresses over the troughs, leading to higher ridge heights and increased lateral roughness variation which enhance in turn the secondary currents. Eventually though, the height and the slope values of

the ridge reach a plateau (Figures 6c–6f), implying that both ridges and troughs erode at the same rate. After this plateau, the ridges' height and side slope continue to decrease, while the troughs stop eroding (Figures 5h–5l). The width of the ridges is found to reach a constant value of $20d_{50}$ (Figure 7b) when the plateau in height and slope is reached.

The lateral positions of the ridges are shown to tend toward an inter-ridge spacing of 1.3 effective water depths (H_e, see Section 3.2.2), which corresponds to the transverse ridge wavelength (Λ_{Col}) theoretically derived by Colombini and Parker (1995) through linear stability analysis. Given that the studies of McLelland et al. (1999) and Scherer et al. (2022) on ridge development without immobile roughness find similar ridge spacings, the results show that the presence of immobile roughness does not influence the lateral spacing of the ridges, as hypothesized.

The number of ridges developing on the bed N_r can be predicted on the basis of the effective water depth and in particular the effective width of the channel (W_e) which results from the reduction of the actual width of the channel induced by the side-wall accumulations, as seen in Table 4. N_r results from the integer part of the number of Λ_{Col}-wavelengths (N_Λ) which fit into the effective width of the channel: $N_r = N_\Lambda - 1$ ($= W_e/\Lambda_{Col} - 1$). Fractional parts of N_Λ in the range (0.1, 0.9) lead to ridge spacings departing from $1.3H_e$ as the result of a higher degree of freedom in the lateral distribution of the ridges. Furthermore, if the fractional part of N_Λ is in the subrange [0.5, 0.9), the development of secondary highly unstable shallow ridges is possible, which eventually disappear however (as in Exp. 1a downstream and Exp. 1b in Figures 5b and 5c). Thus, non-integer N_Λ could explain spacings of $2H$ to $3H$ observed in previous studies (Hirano & Ohmoto, 1988; Ikeda, 1981; Nezu et al., 1988; Wolman & Brush, 1961). For example, the topographic data by Hirano and Ohmoto (1988) show the development of two ridges with a lateral spacing of $2H$ in an uniform sediment bed with an effective width of 24 cm and a water depth of 4.9 cm corresponding to a non-integer number of Λ_{Col}-wavelengths equal to 3.7. This suggests that the number of ridges developing over uniform fine-sediment bed can also be predicted on the basis of Λ_{Col}-wavelengths if the effective width of the channel is used. Overall, the prediction of the number of ridges requires the width of the side-wall accumulations which are not known a priori and need to be estimated. However, for very high aspect ratios, the effective width approaches the actual width.

Recent experimental and numerical studies by Vanderwel and Ganapathisubramani (2015) and by Hwang and Lee (2018), respectively, observed that by varying the lateral spacing between immobile artificial ridges, the strongest secondary currents developed for spacings equal to 1.18 boundary layer thicknesses δ (with no other spacings tested between 1.18 and 1.76 δ). In a similar manner, an experimental wind tunnel study by Wangsawijaya et al. (2020) over heterogeneous roughness stripes, identified the strongest secondary current for a spacing equal to 1.24δ. These spacings are close to the lateral wavelengths observed here. We therefore conjecture that ridges rearrange themselves in natural river systems to reach this characteristic lateral spacing as the intensity of the secondary currents is maximized herewith. The observed spacing can in turn be associated with the maximum friction factor as observed by Zampiron et al. (2020): by varying the width and the height of fixed ridges, the authors found that a peak in friction factor occurs for ridge spacings comprised between 1.1 and 1.6 water depths which encompasses the spacing found here. The naturally-developing lateral spacing of $1.3H_e$ observed herein is therefore in accordance with the ridge spacing which maximizes the energy dissipation of the system by increasing the intensity of the secondary currents. As hypothesized by Davies and Sutherland (1983), channels have a tendency to self-adjust their geometry to achieve the maximum friction factor and minimize herewith the energy of the system (Huang et al., 2004).

The ridges affect the secondary currents not only when they are elevated compared to the surrounding bed, as previous studies on artificial ridges showed (Medjnoun et al., 2020; Wang & Cheng, 2006), but also when they are recessed below large immobile grains. In this case, the ridges influence the secondary current via both topographical and roughness variations depending on the protrusion level, as hypothesized. In particular, for covered spheres and low protrusion levels over the ridges ($-0.2 < P < 0.4$), the intensity of the secondary current is mainly driven by the ridge height, while the lateral roughness variations remain unaltered (Figure 15b). On the contrary, for high protrusion levels ($P > 0.4$), the secondary current is affected mainly by the lateral roughness heterogeneity. The decrease in the ridge height for low P and the decrease in the lateral roughness heterogeneity for high P induce a reduction of the upflow over the ridge and an increase in the streamwise velocity at the water surface.

The combined influence of the ridge topography and of the lateral roughness heterogeneity on the flow is particularly evident in the intensity of the secondary currents, which can be characterized by upflow values as high as 6% of the maximum streamwise velocity (Figure 14d). This upflow value is much higher than the ones usually observed for secondary currents developing in open-channels with smooth or rough beds (Albayrak & Lemmin, 2011; Nezu et al., 1985; Tominaga et al., 1989), over smooth artificial ridges (Nezu & Nakagawa, 1984; Wang & Cheng, 2006) or over ridges in weakly bimodal sediment beds (McLelland et al., 1999), where maximum values of 1.5%–3% are observed. Therefore, the concomitant presence of ridges and strong lateral roughness variations leads to stronger secondary currents with very pronounced curvatures in the turbulent shear stress profiles (Figure 14f).

The higher intensity of the secondary currents associated with ridges developing over an immobile rough bed also explains the observed maximum ridge heights as high as $4d_{50}$ (Figure 7a). This is significantly higher than the one observed for ridges developing over a weakly bimodal sediment bed of about $1d_{50}$ (McLelland et al., 1999).

The higher erosion rates observed over the troughs than over the ridges are in accordance with the higher shear stress conditions observed over the troughs than over the ridges (Figure 14f). The difference in shear stress conditions, in turn, is coupled to differences in the local vertical structure of the turbulence. A quadrant analysis applied over the ridges and over the troughs (Appendix B), shows that the downflow taking place over the troughs concentrates the most intense sweeps in the near-bed region leading to higher local erosion. Over the ridges, on the other hand, the upflow causes the sweep events with the highest intensity to be displaced higher up into the bulk flow to approximately 20% of the water depth, leading to reduced local erosion.

4.3. Erosive Regimes Induced by Changes in Protrusion

The local analysis of the protrusion of the spheres has revealed similar erosive trends over the ridges and the troughs. While previous studies on fine sediment erosion from immobile rough beds (Grams & Wilcock, 2014; Kuhnle et al., 2013, 2016) argued that the area covered by fine sediments is the primary control of the bed erosion, it is shown here that the erosion rates are dominated by changes in the protrusion levels of the spheres (Figures 11c and 11d). The effect of the area coverage is just to slightly dampen the erosion rates without modifying the erosive trends. Four erosive regimes were identified, i.e., an initial decrease in erosion rates, followed by an erosion enhancement and subsequent decrease until negligible erosion rates are reached with increasing protrusion levels. As hypothesized, the regime changes are controlled by critical protrusion levels.

In the first regime of decaying erosion rate for $P < P_{c1}(\simeq 0.2)$, the protruding spherical caps are relatively shallow. The absence of scour holes and sediment shadows suggests that horseshoe vortices have not yet formed. The decaying erosion rate is evidently a sheltering effect due to the increasing drag exerted by the spheres on the flow as P increases. We therefore name this erosive regime the *drag sheltering regime*.

The transition to the second regime occurs at a protrusion level $P_{c1} \simeq 0.2$ (Figure 12a) and can be related to the initiation of flow separation around the spheres as follows. By defining the angle of attack for a protruding spherical cap on the basis of the ratio between the protruding height and the planar radius measured at half height, as done in the case of hills (Ferreira et al., 1995), the critical protrusion level P_{c1} corresponds to an angle of attack of approximately 25°–30°, for which the development of horseshoe vortices was observed for cylinders, cones and spherical caps investigated for varying inclinations, side-slopes and protrusion levels, respectively (Euler et al., 2014; Okamoto et al., 1977; Raus, 2019). Furthermore, for a square pattern of spherical caps over an immobile flat rough bed, Raus et al. (2019) observed the development of a shear layer at the top of the spheres for $P = 0.2$, which reaches the underlying bed causing locally enhanced turbulence. The increase in erosion rate observed for $P_{c1} < P < P_{c2}$ can be connected to an increase in shear-layer intensity, which Raus et al. (2019) showed to increase with P. It is further expected that the intensity of the horseshoe vortex increases as the induced scour hole deepens, as observed in scouring processes around vertical cylinders (Dey & Raikar, 2007; Muzzammil & Gangadhariah, 2003), contributing to the erosion-rate enhancement. The local maximum erosion rate E_{c2} is reached at the next transition ($P = P_{c2}$). Due to the increased shear stresses, E_{c2} can even exceed the erosion rate E_0 observed when the spheres start to protrude, i.e., $E_{c2}/E_0 > 1$ (Figure 12i). The second regime for $P_{c1} < P < P_{c2}$ is, therefore, defined as a *turbulence-enhancement regime*.

It should be noted that previous experimental studies on fine-sediment erosion from a rough immobile bed deduced an increase in sediment transport rates when the immobile roughness elements start to protrude from the

fine-sediment bed (Grams & Wilcock, 2007; Nickling & McKenna Neumann, 1995). Here, it is shown that the enhancement in erosion and consequently in sediment transport does not take place immediately after the spheres start to protrude, but only after a critical protrusion level ($P_{c1} \simeq 0.2$) is surpassed.

The transition to the third regime, characterized by a peak in erosion rate, occurs at $P_{c2} \simeq 0.4$ (Figure 12a), which corresponds to a planar density $\lambda_p \simeq 0.3$. This value of λ_p is identified by Grimmond and Oke (1999) as the threshold condition for the transition from isolated to wake-interference flow conditions in the canopy region in the context of urban canopies. According to the definition of Morris (1955), the flow in the canopy region can be considered isolated as long as the wake of a roughness element dissipates before the next one. As soon as the wake interacts with the downstream roughness element, wake-interference flow conditions are given. As shown by Raus et al. (2019) for a pattern of hemispheres in an open-channel flow or by Liu et al. (2019) and Ferreira et al. (1995) for hills, the size of the recirculation region in the obstacles' lee side increases with increasing height of the obstacles. It can therefore be deduced that the second regime ($P_{c1} < P < P_{c2}$) is an isolated wake flow. In the second regime, as the protrusion of the spheres increases, the reattachment point of the recirculation region moves downstream, eventually reaching the downstream sphere for $P = P_{c2} \simeq 0.4$. Then, in the third regime for $P_{c2} < P < P_{c3}$, the flow becomes a wake-interference regime with a recirculation region characterized by increasingly reduced bed shear-stress conditions, i.e., sheltering, reducing the erosion rates. The third regime can therefore be described as a *wake-interference sheltering regime*.

Over the ridges, the first and second transition take place at lower protrusion levels than over the troughs (Figure 12b). This difference is likely due to the different topographic features between ridges and troughs: while the sediment levels are quite homogeneous around the spheres located in the trough, the spheres at the ridge protrude in an asymmetric manner, with higher bed levels observed toward the ridge crest due to the transverse up-sloping bed. This asymmetry might cause non-uniform flow conditions at the level of the spheres which erode faster on one side showing lower protrusion levels for the first transition. Further studies are necessary to confirm this difference.

The transition to the fourth regime is defined when the erosion rate reaches 0.5% of the initial erosion rate E_0, i.e., a very low erosion rate. On both the troughs and the ridges, it is observed to occur for protrusion levels $P_{c3} \simeq 0.7$ (Figures 12a and 12b), corresponding to a planar density $\lambda_p \simeq 0.5$. This planar density corresponds, in turn, to the transition between a wake-interference and a skimming flow regime, as observed by Grimmond and Oke (1999) in urban canopies. The skimming flow regime is characterized by the persistence of stable vortices filling completely the interstitial region between the roughness elements, thereby disconnecting the flow in between the roughness elements from the outer flow (Leonardi et al., 2003; Placidi & Ganapathisubramani, 2015). Experimental and numerical studies (Leonardi & Castro, 2010; MacDonald et al., 2016; Placidi & Ganapathisubramani, 2015; Raupach et al., 1980) have shown that the transition between wake-interference and skimming flow is characterized by a peak in drag acting on the bed. As a result, the shear stress acting on the fine sediments, resulting from the difference between the total shear stress and the drag in a shear stress partitioning framework (Raupach, 1992; Yager et al., 2007), reaches a minimum, leading to a significant damping of the erosion rates (Figures 11c and 11d). The fourth regime for $P > P_{c3}$ can therefore be described as a *skimming-flow sheltering regime*. For Exp. 1a/b, Exp. 4, and Exp. 5a/b, all characterized by a final quasi-stable bed in the range $0.75 < P < 0.8$ at locations where the fourth erosive regime has been reached (Figures 5a–5c, and Figures 5h–5j), the reduction in shear stress acting on the fine sediments is evidently enough to reach critical conditions of motion. For Exp. 2 and 3 though, with medium and high Shields parameters θ, the reduction in shear stress taking place when skimming flow conditions set in, is not enough to reach critical conditions of motion before the bed fully erodes. Regardless of the driving shear stress, the skimming flow conditions for $P > P_{c3}$ imply a significantly reduced erosion rate. In other words, skimming flow conditions are a necessary but not sufficient condition for the bed to reach a stable sediment level.

The three critical protrusion levels are found to be essentially independent of the Shields parameter θ and of the aspect ratio A for both the troughs and the ridges (Figures 12a and 12b). The independence supports the underlying assumption that the change in erosive regimes is mainly driven by changes in the local flow dynamics due to the evolving geometry as the spheres increasingly protrude. For the first transition, it appears to be the critical angle necessary to induce the formation of a horseshoe vortex and of a shear layer, while for the second and third transition, it is the planar density. Consequently, the erosion of fine sediments from natural immobile rough beds such as gravel is also expected to be driven by the geometric features of the bed with similar results. Natural rough

beds can be geometrically characterized on the basis of the roughness geometry function, $\phi_p(z)$, which represents the percentage of area occupied by fluid at a certain elevation within the bed interstices (Aberle, 2007; Nikora et al., 2001) and which can be related to the planar density of the immobile grains via $\lambda_p = 1 - \phi_p(z)$. Laser scans of natural gravel beds along with flow measurements in the bed interstices could yield the necessary information for further studies to corroborate the observed erosive regimes.

5. Conclusions

The erosion of an initially uniform fine-sediment bed covering a rough bed composed of immobile spheres has been analyzed by topographic and PIV measurements in a laboratory flume to assess the influence of immobile grains on the local erosion rates and on the morphodynamics of sediment ribbons under sediment-supply-limited conditions. As soon as the immobile spheres protrude, sediment ribbons are observed to develop for shear stress conditions higher than the threshold for which they are observed over uniform fine-sediment beds. The long-term morphological evolution of the sediment ribbons is quantified for the first time. The fine sediments are eroded more quickly in the troughs than over the ridges, so that the troughs reach a constant sediment bed level well before the ridges. The ridges are characterized by an initial growth phase which leads to maximum heights of up to $4d_{50}$. Their ensuing decay is characterized by a constant width equal to approximately $20d_{50}$. The natural lateral spacing of the ridges is found to be equal to 1.3 effective water depth H_e, on the basis of which the number of developing ridges can be determined once the reduction of the channel width by the side-wall accumulations is taken into account.

The concomitant presence of the lateral topographic variations induced by the ribbons and of the lateral roughness heterogeneity due to the associated variation in protrusion of the spheres, induce a strengthening of the secondary currents as compared to uniform beds. The secondary currents, whose intensity reduces as the ridges disappear over time, are affected by variations of the ridge height for low protrusion levels of the spheres, while for high protrusion levels they are mainly affected by the variation in lateral roughness heterogeneity.

The longevity of the sediment ribbons can be ascribed to the secondary currents which locally reduce or enhance the shear stress conditions. However, independently of the local shear stress conditions, both ridges and troughs display similar erosive behaviors with the same alternation of erosion reducing (sheltering) and enhancing conditions with increasing protrusion of the spheres, i.e., the immobile roughness elements. The influence of secondary currents and of roughness elements on the erosion of fine sediments can be therefore treated as partially decoupled phenomena, the first ones providing the forcing for the second ones. The redistribution of momentum by the secondary currents only influences the magnitude of the local erosion but not the erosive behavior and regimes which are dominated by the protrusion of the immobile roughness elements.

The present experiments allowed the competition and apparent contradiction between erosion enhancement and grain sheltering induced by protruding roughness elements, to be clarified. Four erosive regimes, common for both ridges and troughs, are identified and found to depend solely on the protrusion level P of the spheres. An initial *drag sheltering regime* is identified when the spheres start to protrude, characterized by decreasing erosion rates due to the increasing drag of the increasingly protruding spheres ($0 < P < 0.2$). A second *turbulence-enhancement regime*, characterized by increasing erosion rates, is identified for protrusion levels for which a horseshoe vortex or a shear layer develop ($0.2 < P < 0.4$). A subsequent reduction in erosion rates is observed and identified as a *wake-interference sheltering regime* ($0.4 < P < 0.7$). The final regime, characterized by very low erosion rates, was identified as a *skimming-flow sheltering regime* ($P > 0.7$). The critical protrusion levels for the transition in erosive regimes are found to be independent of the Shields parameter and the flow aspect ratio, at least for the ranges investigated ($0.11 < \theta < 0.18$ and $2.9 < A < 6.5$). Instead, they can be seen to be driven by the canopy flow as the canopy's geometry evolves with P. The first transition in erosive behavior takes place when a critical angle of attack of 25°–30° is reached, while for the second and third transitions, the change in flow/erosive regime can be related to the planar density of the roughness elements, $\lambda_p = 0.3$ and $\lambda_p = 0.5$, respectively. These critical values of the angle of attack and of the planar density are expected to hold for other configurations of immobile grains. The newly identified flow regimes can be used to improve erosion models which currently simply consider grain sheltering (e.g., Stradiotti et al., 2020).

In the final sheltering regime beyond P_{c3}, an effectively stable bed with only occasional grain movement is eventually reached since the erosion rates become vanishingly small with increasing P. This final or equilibrium bed

level lies in the range of $0.75 < P < 0.8$ for all low Shields numbers investigated except for Exp. 2 and 3 with higher Shields numbers, which were completely eroded, evidently under the influence of the glass plate below. While the transition to the skimming flow sheltering regime P_{c3} is independent of the Shields parameter, the fact that Exp. 2 and 3 erode completely in contrast to the others, suggests a Shield dependence of the final erosion depth, in agreement with previous studies on the erosion depth in gravel beds (Kuhnle et al., 2016; Stradiotti et al., 2020). This Shields dependence is, however, not as large as the observed complete erosion suggests, which was clearly influenced by the glass plate. For the other experiments (Exp. 1a/b, 4, and 5a/b), where the final bed level lies in the range given above, a Shields dependence is difficult to determine due to the measurement uncertainty as well as the restricted measurement times which can both hide a small Shield dependence. For gravel beds, this implies that as long as the critical shear stress to set the gravel grains into motion is not exceeded, fine-sediments are eroded until a certain depth, the final erosion depth. This occurs for protrusion levels higher than P_{c3}, which can therefore be used as a first estimate of the minimum final erosion depth for flushing flow measures for the removal of superficial and interstitial fine sediments in gravel beds. More experiments are necessary to determine the final depth for higher Shields parameters up to critical motion of the gravel and with a deeper bed.

It should be noted that the sheltering conditions induced by the spheres in the final regime feed back to the bedform scale since the topographic variations due to ridges are leveled out to a quasi-uniform bed. Thus, the initial bedform signature of the secondary currents, i.e., the ribbons, is not evident anymore. The protruding roughness elements decouple as such the secondary flow from the flow within the canopy.

In addition to extending this study to natural gravel beds in order to confirm the erosive regimes and extend the final bed-level dependence on the Shields parameter, further studies are needed which combine the hydrodynamics of the canopy flow with the morphodynamics of the eroding bed. These should allow the relationship between the total shear stress and the shear stress acting on the fine sediments to be better understood and thereby provide the basis for better erosion models.

Appendix A: Derivation of the Exner Equation Over an Immobile Rough Bed

In the presence of immobile roughness elements protruding from the bed, the fine-sediment part of the bed surface changes with the protrusion level. To address this, consider the control volume V_c with surface S_c in Figure A1, spanning one pattern width. The lower surface of the control volume is mobile and follows the variations in the average sediment bed level z_b which moves with a velocity $u_b = \partial_t z_b$ or equivalently in terms of the average protrusion level P ($=-z_b/R$) with $u_b = -R\partial_t P$. The conservation of the total sediment mass in V_c can be expressed as follows:

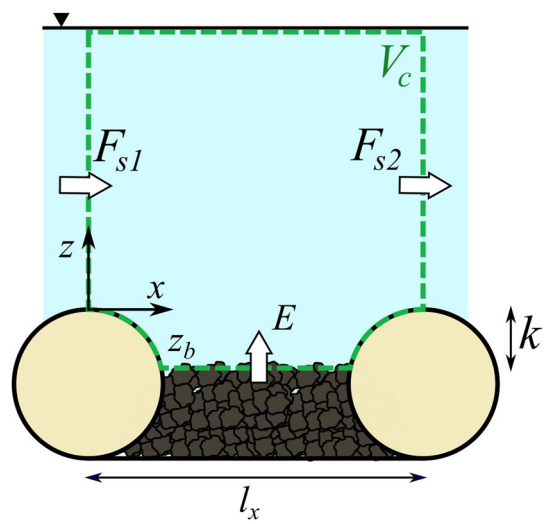

Figure A1. Definition of the control volume V_c with sediment fluxes from the bed E and through the vertical surfaces of the control volume F_s.

$$\frac{dm_s}{dt} = \frac{d}{dt}\int_{V_c} (\rho_s c)\, dV_c = 0, \tag{A1}$$

where c represents the concentration of sediments (both suspended or part of the bed matrix). By applying the Reynolds transport theorem, Equation A1 can be cast in the following form:

$$\int_{V_c} \frac{\partial (\rho_s c)}{\partial t} dV_c + \int_{S_c} (\rho_s c)\, \vec{u} \cdot d\vec{S}_c = 0, \tag{A2}$$

where $\vec{u}$ is the advection velocity of the sediments. The first term in Equation A2 represents the variation of suspended sediments within the control volume, which can be considered negligible in the presence of bedload. The momentum balance therefore reduces to the second term in Equation A2, given by the flux of sediments $F_{s,i}$ entering and leaving the control volume and by the flux of sediments E through the fine-sediment bed surface S_b (Figure A1). E can be expressed as follows:

$$E = \int_{S_b} (\rho_s C u_b)\, dS_b \tag{A3}$$

where C is the concentration of the fine sediments in the bed (solidity) and $S_b = S_r - S_p = (1 - \lambda_p) l_x l_y$ the fine-sediment bed surface (with S_r and S_p as defined in Section 2.2). Given that all quantities here are pattern-averaged, C and u_b are taken as averages over S_b so that Equation A3 yields:

$$E = -\rho_s (1 - \lambda_p) C R \frac{\partial P}{\partial t} l_x l_y. \tag{A4}$$

Similarly, with an average volumetric sediment transport rate $Q_{s,i} = \int_{S_{v,i}} (cu) dS_{v,i}$ through the vertical control surfaces $S_{v,i}$ of the control volume, the net streamwise sediment flux $\Delta F_s = F_{s,2} - F_{s,1}$ can be expressed as:

$$\Delta F_s = \rho_s \Delta Q_s \tag{A5}$$

The conservation of mass, $\Delta F_s + E = 0$, can be then written as

$$\frac{\Delta q_s}{l_x} - (1 - \lambda_p) C R \frac{\partial P}{\partial t} = 0, \tag{A6}$$

where $q_s = Q_s / l_y$ is the sediment transport rate per unit width. Considering the pattern average as a local quantity, conservation of mass on the pattern scale becomes

$$\frac{\partial q_s}{\partial x} - (1 - \lambda_p) C R \frac{\partial P}{\partial t} = 0, \tag{A7}$$

where the longitudinal gradient is understood on the pattern scale consistent with the definition of P. The term $1 - \lambda_p$, corresponding to the percentage of area covered by fine sediments, reflects the reduced availability of sediments due to the presence of roughness elements. The second term in Equation A7 represents the total erosion rate from the bed, denoted as E_t. This erosion rate does not give an estimate of the sediment transport rate, but of the longitudinal variability of the sediment fluxes through the control volume. As such, the erosion rates are a proxy of whether equilibrium sediment transport conditions are present.

It can be noted that in the absence of protruding immobile roughness elements $\lambda_p = 0$, the Exner equation for a uniform fine-sediment bed is retrieved:

$$\frac{\partial q_s}{\partial x} - C R \frac{\partial P}{\partial t} = 0. \tag{A8}$$

Appendix B: Quadrant Analysis Over the Ridges and the Troughs

A quadrant analysis is performed for Exp. 5b both in the middle and in the quarter plane for the time instants t_1 and t_3. Quadrant analysis decomposes the Reynolds shear stress in the contributions from different turbulent events, identified in the u'–w' plane (Lu & Willmarth, 1973; Raupach, 1981). Each quadrant in the u'–w' plane

is associated with an event: Q1-outward interaction ($u' > 0$, $w' > 0$), Q2-ejections ($u' < 0$, $w' > 0$), Q3-inward interactions ($u' < 0$, $w' < 0$), and Q4-sweep ($u' > 0$, $w' < 0$). The time fraction of the ith-quadrant event and its contribution to the Reynolds shear stress at a single point in space is given by:

$$T_{i,H_s} = \frac{1}{T}\int_0^T I_{i,H_s}\,dt \tag{B1}$$

$$\overline{u'w'}_{i,H_s} = \frac{1}{T}\int_0^T u'w'(x,z,t)I_{i,H_s}\,dt \tag{B2}$$

where T is the sampling duration and I_{i,H_s} the indicator function. Consistent with a double-averaged framework, the indicator function is defined on the basis of the double-averaged shear stress $-\rho_f\langle\overline{u'w'}\rangle_x(z)$, as in Mignot et al. (2009):

$$I_{i,H_s} = \begin{cases} 1, \text{if } (u', w') \text{ is in quadrant } i \text{ and } u'w'(x,z,t) > H_s\langle\overline{u'w'}\rangle_x(z) \\ 0, \text{otherwise} \end{cases} \tag{B3}$$

where H_s is the hole size, which represents a threshold level for the identification of the turbulent events. Here, $H_s = 0$ is chosen, in order to consider all turbulent events.

Figures B1a and B1b illustrate the double-averaged profiles of the normalized intensity of the Reynolds-shear-stress contributions of the turbulent events $\left(-\langle\overline{u'w'}_{i,0}\rangle_x/T_{i,0}\right)/u_{*H}^2$ over the ridges and troughs, respectively. Figure B1a shows that at time t_1, the intensity of the sweeps over the ridge is higher than the intensity of the ejections for $z/H < 0.25$, while the opposite is true for $z/H > 0.25$. At time t_3, the extension of the region dominated by sweeps reduces to a height $z/H \simeq 0.15$, likely as the result of the reduction in the upflow (Figure 14d). At both times, the vertical extent of the region dominated by sweeps is much higher than the one observed over flat rough beds, presumably without secondary currents, which extends at most up to 5% of H (Dey & Das, 2012; Mignot et al., 2009; Raupach, 1981; Sarkar et al., 2016).

Figure B1a further shows that over the ridge, the contribution of sweeps and ejections to the total Reynolds shear stress follows the same vertical trend: the sweep and ejection profiles increase up to $z/H \simeq 0.2$–0.3 and then decrease. This is in contrast with the results over a flat gravel bed by Mignot et al. (2009) and Dey et al. (2012), where the contribution of sweeps and ejections peaks near the top of the roughness. The displacement of the peak in sweep intensity can be attributed to the upflow conditions dominating over the ridges. As a result, the near bed-region is characterized by more quiescent sweeps, with an intensity slightly higher than the critical shear stress conditions defined by the Shields diagram, indicated by a vertical dashed line (Figure B1a). As such, at

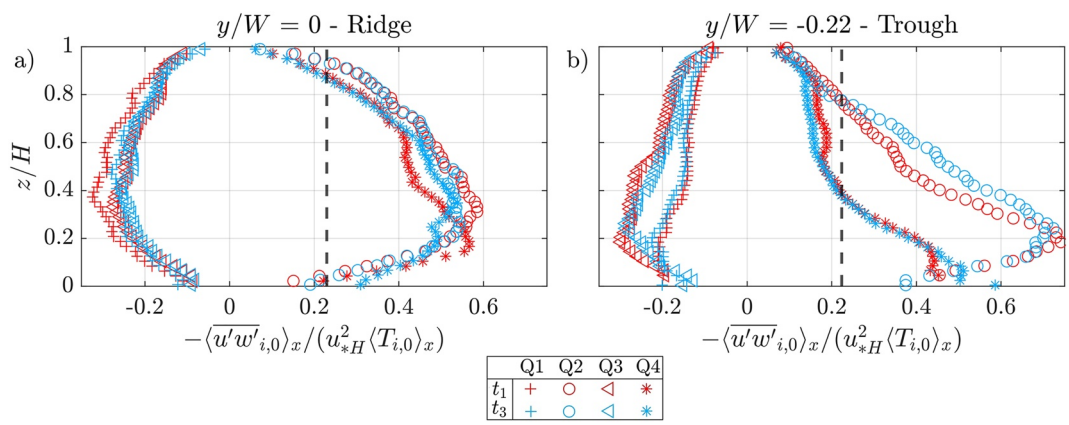

Figure B1. Normalized double-averaged profiles of the intensities of the Reynolds-shear-stress contributions of the turbulent events $\left(-\langle\overline{u'w'}_{i,0}\rangle_x/\langle T_{i,0}\rangle_x\right)/u_{*H}^2$ for Exp. 5b over the ridge (a) and the trough (b). The vertical dashed line represents the critical conditions of motion.

t_1, when the ridge is higher than the top of the spheres (Figure 13b), intermittent sediment transport is possible, even though the average shear stress $-\rho_f \langle \overline{u'w'} \rangle_x$ is below the threshold of movement (Figure 14f). At t_3, the intensity of the sweeps near the bed slightly increases, due to the protruding spheres, but the erosion is damped as the protrusion level $P\,(t = t_3) = 0.65$ (Figure 13b) lies within the range $P_{c2} < P < P_{c3}$ which corresponds to the *wake-interference sheltering regime* (see Section 4.3).

Over the troughs, Figure B1b shows that the sweeps dominate the shear stress production over a narrow region near the top of the spheres for $z/H < 0.05$. Since the intensity of the downflow does not change between the time instants t_1 and t_3 (Figure 14d), the sweeps and ejections profiles are similar between the two times and the transition between the region dominated by sweeps and the one dominated by ejections takes place at approximately the same height ($z/H \simeq 0.05$). Compared to the ridge, the downflow causes the region dominated by sweeps to vertically reduce. The turbulent structure near the bed is, as such, similar to the one observed over flat rough beds (Dey & Das, 2012; Mignot et al., 2009; Sarkar et al., 2016).

Figure B1b further shows that the contribution of the sweep events presents a peak near the bed, while the contribution of the ejections reaches a maximum at $z/H = 0.2$. Compared to the ridge, which shows a peak in sweep intensity of similar magnitude higher above the bed (Figure B1a), the downflow over the troughs displaces the peak near the bed, causing higher erosion rates compared to the ridge. The intensity of the sweeps over the troughs is indeed consistently higher than the critical condition of motion near the bed (Figure B1b). Nevertheless, the erosion is completely suppressed over the troughs at t_3, as the protrusion level $P(t = t_3) = 0.78$ (Figure 13b) is within the *skimming-flow sheltering regime*, i.e., $P \geq P_{c3}$ (see Section 4.3).

Data Availability Statement

All experimental data used in this paper are part of a Zenodo open data file (https://doi.org/10.5281/zenodo.5787371).

Acknowledgments
The authors thank Dr. T. Revil-Baudard and Prof. M. Tubino for helpful discussions and Dr. T. Revil-Baudard, D. Gross, M. Ziegler, J. Ulrich for the help in the preparation of the experiments. Michele Trevisson's PhD was financially supported by the Landesgraduiertenförderung of the Land Baden-Württemberg (Germany) and by the Graduate School for Climate and Environment (KIT). Open Access funding enabled and organized by Projekt DEAL.

References

Aberle, J. (2007). Measurements of armour layer roughness geometry function and porosity. *Acta Geophysica*, *55*(1), 23–32. https://doi.org/10.2478/s11600-006-0036-5

Akutina, Y., Eiff, O., Moulin, F., & Rouzes, M. (2019). Lateral bed-roughness variation in shallow open-channel flow with very low submergence. *Environmental Fluid Mechanics*, *19*(5), 1339–1361. https://doi.org/10.1007/s10652-019-09678-w

Al-Awadhi, J., & Willetts, B. (1999). Sand transport and deposition within arrays of non-erodible cylindrical elements. *Earth Surface Processes and Landforms*, *24*(5), 423–435. https://doi.org/10.1002/(SICI)1096-9837(199905)24:5<423::AID-ESP998>3.0.CO;2-E

Albayrak, I., & Lemmin, U. (2011). Secondary currents and corresponding surface velocity patterns in a turbulent open-channel flow over a rough bed. *Journal of Hydraulic Engineering*, *137*(11), 1318–1334. https://doi.org/10.1061/(ASCE)HY.1943-7900.0000438

Ashworth, P., & Ferguson, R. (1989). Size-selective entrainment of bed load in gravel bed streams. *Water Resources Research*, *25*(4), 627–634. https://doi.org/10.1029/WR025i004p00627

Bagnold, R. (1966). An approach to the sediment transport problem from general physics. Geological survey professional paper, 422-I.

Bendat, J., & Piersol, A. (2010). *Random data: Analysis and measurement procedures*. Wiley-Interscience. https://doi.org/10.1002/9781118032428

Bose, S., & Dey, S. (2013). Sediment entrainment probability and threshold of sediment suspension: Exponential-based approach. *Journal of Hydraulic Engineering*, *139*(10), 1099–1106. https://doi.org/10.1061/(ASCE)HY.1943-7900.0000763

Carling, P., Gölz, E., Orr, H., & Radecki-Pawlik, A. (2000). The morphodynamics of fluvial sand dunes in the River Rhine, near Mainz, Germany. I. Sedimentology and morphology. *Sedimentology*, *47*(1), 227–252. https://doi.org/10.1046/j.1365-3091.2000.00290.x

Chiew, Y., & Parker, G. (1994). Incipient sediment motion on non-horizontal slopes. *Journal of Hydraulic Research*, *32*(5), 649–660. https://doi.org/10.1080/00221689409498706

Church, M., McLean, D., & Wolcott, J. (1987). River bed gravels: Sampling and analysis. In C. Thorne, J. Bathurst, & R. Hey (Eds.), *Sediment transport in gravel-bed rivers* (pp. 43–88). John Wiley & Sons.

Coleman, S., Nikora, V., McLean, S., & Schicke, E. (2007). Spatially averaged turbulent flow over square ribs. *Journal of Engineering Mechanics*, *133*(2), 194–204. https://doi.org/10.1061/(ASCE)0733-9399(2007)133:2(194)

Coleman, S., Nikora, V. I., & Aberle, J. (2011). Interpretation of alluvial beds through bed-elevation distribution moments. *Water Resources Research*, *47*(11), W11505. https://doi.org/10.1029/2011WR010672

Colombini, M., & Parker, G. (1995). Longitudinal streaks. *Journal of Fluid Mechanics*, *304*, 161–183. https://doi.org/10.1017/S0022112095004381

Culbertson, J. (1967). *Evidence of secondary circulation in an alluvial channel* (pp. D214–D216). US Geological Survey.

Davies, T., & Sutherland, A. (1983). Extremal hypothesis for river behaviour. *Water Resources Research*, *19*(1), 141–148. https://doi.org/10.1029/WR019i001p00141

Dey, S. (2014). *Fluvial hydrodynamics: Hydrodynamic and sediment transport phenomena*. Springer. https://doi.org/10.1007/978-3-642-19062-9

Dey, S., & Das, R. (2012). Gravel-bed hydrodynamica: Double-averaging approach. *Journal of Hydraulic Engineering*, *138*(8), 707–725. https://doi.org/10.1061/(ASCE)HY.1943-7900.0000554

Dey, S., Das, R., Gaudio, R., & Bose, S. (2012). Turbulence in mobile-bed streams. *Acta Geophysica*, *60*(6), 1547–1588. https://doi.org/10.2478/s11600-012-0055-3

Dey, S., & Raikar, R. (2007). Characteristics of horseshoe vortex in developing scour holes at piers. *Journal of Hydraulic Engineering*, *133*(4), 399–413. https://doi.org/10.1061/(ASCE)0733-9429(2007)133:4(399)

Dixen, M., Sumer, B., & Fredsoe, J. (2013). Numerical and experimental investigation of flow and scour around a half-buried sphere. *Coastal Engineering*, *73*, 84–105. https://doi.org/10.1016/j.coastaleng.2012.10.006

Euler, E., Zemke, J., Rodrigues, S., & Herget, J. (2014). Influence of inclination and permeability of solitary woody riparian plants on local hydraulic and sedimentary processes. *Hydrological Processes*, *28*(3), 1358–1371. https://doi.org/10.1002/hyp.9655

Euler, T., & Herget, J. (2012). Controls on local scour and deposition induced by obstacles in fluvial environments. *Catena*, *91*, 35–46. https://doi.org/10.1016/j.catena.2010.11.002

Fang, H., Liu, Y., & Stoesser, T. (2017). Influence of boulder concentration on turbulence and sediment transport in open-channel flow over submerged boulders. *Journal of Geophysical Research: Earth Science*, *122*(12), 2392–2410. https://doi.org/10.1002/2017JF004221

Ferguson, R., Prestegaard, K., & Ashworth, P. (1989). Influence of sand on hydraulics and gravel transport in a braided gravel bed river. *Water Resources Research*, *25*(4), 635–643. https://doi.org/10.1029/WR025i004p00635

Ferreira, A., Lopes, A., Viegas, D., & Sousa, A. (1995). Experimental and numerical simulation of flow around two-dimensional hills. *Journal of Wind Engineering and Industrial Aerodynamics*, *54*, 173–181. https://doi.org/10.1016/0167-6105(94)00040-k

Ghilardi, T., Franca, M., & Schleiss, A. (2014). Sediment transport in steep channels with large roughness elements. *River Flow*, *51*, 5260–5283. https://infoscience.epfl.ch/record/202023

Gillette, D., & Stockton, P. (1989). The effect of nonerodible particles on wind erosion of erodible surfaces. *Journal of Geophysical Research*, *94*(D10), 12885–12893. https://doi.org/10.1029/JD094iD10p12885

Gillies, J., Nickling, W., & King, J. (2006). Aeolian sediment transport through large patches of roughness in the atmospheric inertial layer. *Journal of Geophysical Research*, *111*(F2), F02006. https://doi.org/10.1029/2005JF000434

Graham, D., Reid, I., & Rice, S. (2005). Automated sizing of coarse-grained sediments: Image-processing procedures. *Mathematical Geology*, *37*(1), 1–28. https://doi.org/10.1007/s11004-005-8745-x

Grams, P., & Wilcock, P. (2007). Equilibrium entrainment of fine sediment over a coarse immobile bed. *Water Resources Research*, *43*(10), W10420. https://doi.org/10.1029/2006WR005129

Grams, P., & Wilcock, P. (2014). Transport of fine sediment over a coarse, immobile riverbed. *Journal of Geophysical Research: Earth Surface*, *119*(2), 188–211. https://doi.org/10.1002/2013JF002925

Grimmond, C., & Oke, T. (1999). Aerodynamic properties of urban areas derived from analysis of surface form. *Journal of Applied Meteorology*, *38*(9), 1262–1292. https://doi.org/10.1175/1520-0450(1999)038⟨1262:APOUAD⟩2.0.CO;2

Hirano, M., & Ohmoto, T. (1988). Experimental study on the interaction between longitudinal vortices and sand ribbons. In *Proceedings of the 6th Congress APD-IAHR* (pp. 59–65).

Hofland, B., Battjes, J., & Booij, R. (2005). Measurement of fluctuating pressures on coarse bed material. *Journal of Hydraulic Engineering*, *131*(9), 770–781. https://doi.org/10.1061/(ASCE)0733-9429(2005)131:9(770)

Hovmöller, E. (1949). The trough-and-ridge diagram. *Tellus*, *1*(2), 62–66. https://onlinelibrary.wiley.com/doi/10.1111/j.2153-3490.1949.tb01260.x

Huang, H., Chang, H., & Nanson, G. (2004). Minimum energy as the general form of critical flow and maximum flow efficiency and for explaining variations in river channel pattern. *Water Resources Research*, *40*(4), W04502. https://doi.org/10.1029/2003WR002539

Hwang, H., & Lee, J. (2018). Secondary flows in turbulent boundary layers over longitudinal surface roughness. *Physical Review Fluids*, *3*(1), 014608. https://doi.org/10.1103/PhysRevFluids.3.014608

Ikeda, S. (1981). Self-formed straight channels in sandy beds. *Journal of the Hydraulics Division ASCE*, *107*(4), 389–406. https://doi.org/10.1061/jyceaj.0005644

Iversen, J., Wang, W., Ramussen, K., Mikkelsen, H., & Leach, R. (1991). Roughness element effect on local transport and universal saltation transport. *Acta Mechanica*, *2*, 65–75. https://doi.org/10.1007/978-3-7091-6703-8_5

Karcz, I. (1966). Secondary currents and the configuration of a natural stream bed. *Journal of Geophysical Research*, *71*(12), 3109–3112. https://doi.org/10.1029/JZ071i012p03109

Kironoto, B., & Graf, W. (1995). Turbulence characteristics in rough uniform open-channel flow. *Proceedings of the Institution of Civil Engineers-Water Maritime and Energy*, *106*(4), 333–344. https://doi.org/10.1680/iwtme.1994.27234

Kleinhans, M. (2002). *Sorting out sand and gravel sediment transport and deposition in sand-gravel bed rivers (doctoral dissertation)*. Faculty of Geographical Sciences, Utrecht University. Retrieved from https://dspace.library.uu.nl/handle/1874/545

Kleinhans, M., Wilbers, A., De Swaaf, A., & Van Den Berg, J. (2002). Sediment supply-limited bedforms in sand-gravel bed rivers. *Journal of Sedimentary Research*, *72*(5), 629–640. https://doi.org/10.1306/030702720629

Kuhnle, R., Wren, D., & Langendoen, E. (2016). Erosion of sand from a gravel bed. *Journal of Hydraulic Engineering*, *142*(2), 04015052. https://doi.org/10.1061/(ASCE)HY.1943-7900.0001071

Kuhnle, R., Wren, D., Langendoen, E., & Rigby, J. (2013). Sand transport over an immobile gravel substrate. *Journal of Hydraulic Engineering*, *139*(2), 167–176. https://doi.org/10.1061/(ASCE)HY.1943-7900.0000615

Le Bouteiller, C., & Venditti, J. (2015). Sediment transport and shear stress partitioning in a vegetated flow. *Water Resources Research*, *51*(4), 2901–2922. https://doi.org/10.1002/2014WR015825

Lenzi, M. (2004). Displacement and transport of marked pebbles, cobbles and boulders in a steep mountain stream. *Hydrological Processes*, *18*(10), 1899–1914. https://doi.org/10.1002/hyp.1456

Leonardi, I., & Castro, S. (2010). Channel flow over large cube roughness: A direct numerical simulation study. *Journal of Fluid Mechanics*, *651*, 519–539. https://doi.org/10.1017/S002211200999423X

Leonardi, S., Orlandi, P., Smalley, R., Djendi, L., & Antonia, R. (2003). Direct numerical simulation of turbulent channel flow with transverse square bars on one wall. *Journal of Fluid Mechanics*, *491*, 229–238. https://doi.org/10.1017/S0022112003005500

Liu, Z., Hu, Y., & Wang, W. (2019). Large eddy simulations of the flow field over simplified hills with different roughness conditions, slopes and hill shapes: A systematical study. *Energies*, *12*(3413), 3413. https://doi.org/10.3390/en12183413

Lu, S. S., & Willmarth, W. W. (1973). Measurements of the structure of the Reynolds stress in a turbulent boundary layer. *Journal of Fluid Mechanics*, *60*(3), 481–511. https://doi.org/10.1017/S0022112073000315

MacDonald, M., Chan, L., Chung, D., Hutchins, N., & Ooi, A. (2016). Turbulent flow over transitionally rough surfaces with varying roughness densities. *Journal of Fluid Mechanics*, *804*, 130–161. https://doi.org/10.48550/arXiv.2012.04130

Marshall, J. (1971). Drag measurements in roughness arrays of varying density and distribution. *Agricultural Meteorology*, *8*, 269–292. https://doi.org/10.1016/0002-1571(71)90116-6

McKenna Neuman, C., & Nickling, W. (1995). Aeolian sediment flux decay: Non-linear behaviour on developing deflation lag surfaces. *Earth Surface Processes and Landforms*, *20*, 423–435. https://doi.org/10.1002/esp.3290200504

McKenna Neuman, C., Sanderson, R. S., & Sutton, S. (2013). Vortex shedding and morphodynamic response of bed surfaces containing non-erodible roughness elements. *Geomorphology*, *198*, 45–56. https://doi.org/10.1016/j.geomorph.2013.05.011

McLean, S. (1981). The role of non-uniform roughness in the formation of sand ribbons. *Marine Geology*, *42*(1–4), 49–74. https://doi.org/10.1016/0025-3227(81)90158-4

McLelland, S., Ashwoth, P., Best, J., & Livesey, J. (1999). Turbulence and secondary flow over sediment stripes in weakly bimodal bed material. *Journal of Hydraulic Engineering*, *125*(5), 463–473. https://doi.org/10.1061/(ASCE)0733-9429(1999)125:5(463)

Medjnoun, T., Vanderwel, C., & Ganapathisubramani, B. (2020). Effects of heterogeneous surface geometry on secondary flows in turbulent boundary layers. *Journal of Fluid Mechanics*, *886*, A31. https://doi.org/10.1017/jfm.2019.1014

Mignot, E., Hurther, D., & Barthelemy, E. (2009). On the structure of shear stress and turbulent kinetic energy flux across the roughness layer of a gravel-bed channel flow. *Journal of Fluid Mechanics*, *638*, 423–452. https://doi.org/10.1017/S0022112009990772

Monin, A., & Yaglom, A. (1971). *Statistical fluid mechanics: Mechanics of turbulence* (Vol. 1). MIT press.

Morris, H. (1955). Flow in rough conduits. *Transactions of the American Society of Civil Engineers*, *120*(1), 373–398. https://doi.org/10.1061/TACEAT.0007206

Muzzammil, M., & Gangadhariah, T. (2003). The mean characteristics of horseshoe vortex at a cylindrical pier. *Journal of Hydraulic Research*, *41*(3), 285–297. https://doi.org/10.1080/00221680309499973

Nelson, J., McLean, R., & Drake, T. (1995). Role of near-bed turbulence structure in bed load transport and bed form mechanics. *Water Resources Research*, *31*(8), 2071–2086. https://doi.org/10.1029/95WR00976

Nezu, I., & Nakagawa, H. (1984). Cellular secondary currents in straight conduit. *Journal of Hydraulic Engineering*, *110*(2), 173–193. https://doi.org/10.1061/(ASCE)0733-9429(1984)110:2(173)

Nezu, I., & Nakagawa, H. (1989). Self forming mechanism of longitudinal sand ridges and troughs in fluvial open-channel flows. In *Proceedings of the 23rd IAHR Congress* (pp. B65–B72).

Nezu, I., & Nakagawa, H. (1993). Turbulence in open-channel flows. IAHR/AIRH Monograph.

Nezu, I., Nakagawa, H., & Kawashima, N. (1988). Cellular secondary currents and sand ribbons in fluvial channel flows. In *Proceedings of the 6th Congress of Asian and Pacific Regional Division, IAHR, II-1* (pp. 51–58).

Nezu, I., Nakagawa, H., & Tominaga, A. (1985). Secondary currents in a straight channel flow and the relation to its aspect ratio. *Turbulent shear flows*, *4*, 246–260. https://doi.org/10.1007/978-3-642-69996-2_20

Nezu, I., & Rodi, W. (1985). Experimental study on secondary currents in open channel flow. In *Proceedings of the 21st IAHR Congress* (pp. 115–119).

Nickling, W., & McKenna Neumann, C. (1995). Development of deflation lag surfaces. *Sedimentology*, *42*(3), 403–414. https://doi.org/10.1111/j.1365-3091.1995.tb00381.x

Nikora, V., Goring, D., & Biggs, B. (1998). Silverstream eco-hydraulics flume: Hydraulic design and tests. *New Zealand Journal of Marine & Freshwater Research*, *32*(4), 607–620. https://doi.org/10.1080/00288330.1998.9516848

Nikora, V., Goring, D., McEwan, I., & Griffiths, G. (2001). Spatially averaged open-channel flow over rough bed. *Journal of Hydraulic Engineering*, *127*(2), 123–133. https://doi.org/10.1061/(ASCE)0733-9429(2001)127:2(123)

Okamoto, T., Yagita, M., & Kataoka, S. (1977). Flow past cone placed on flat plate. *Bulletin of the Japan Society of Mechanical Engineers*, *20*(141), 329–336. https://doi.org/10.1299/jsme1958.20.329

Papanicolaou, A., Dermisis, D., & Elhakeem, M. (2011). Investigating the role of clasts on the movement of sand in gravel bed rivers. *Journal of Hydraulic Engineering*, *137*(9), 871–883. https://doi.org/10.1061/(ASCE)HY.1943-7900.0000381

Papanicolaou, A., Kramer, C., Tsakiris, A., Stoesser, T., Bomminayuni, S., & Chen, Z. (2012). Effects of a fully submerged boulder within a boulder array on the mean and turbulent flow fields: Implications to bedload transport. *Acta Geophysica*, *60*(6), 1502–1546. https://doi.org/10.2478/s11600-012-0044-6

Pattenden, R., Turnock, S., & Zhang, X. (2005). Measurements of the flow over low-aspect-ratio cylinder mounted on a ground plane. *Experiments in Fluids*, *39*(1), 10–21. https://doi.org/10.1007/s00348-005-0949-9

Pitlick, J. (1993). Response and recovery of a subalpine stream following a catastrophic flood. *GSA Bulletin*, *105*(5), 657–670. https://doi.org/10.1130/0016-7606(1993)105⟨0657:RAROAS⟩2.3.CO;2

Placidi, M., & Ganapathisubramani, B. (2015). Effects of frontal and plan solidities on aerodynamic parameters and the roughness sublayer in turbulent boundary layers. *Journal of Fluid Mechanics*, *782*, 541–566. https://doi.org/10.1017/jfm.2015.552

Powell, D. (2014). Flow resistance in gravel-bed rivers: Progress in research. *Earth-Science Reviews*, *136*, 301–338. https://doi.org/10.1016/j.earscirev.2014.06.001

Powell, D., Reid, I., & Laronne, J. (2001). Evolution of bed load grain size distribution with increasing flow strength and the effect of flow duration on the caliber of bed load sediment yield in ephemeral gravel bed rivers. *Water Resources Research*, *37*(5), 1463–1474. https://doi.org/10.1029/2000WR900342

Raupach, M. (1981). Conditional statistics of Reynolds stress in rough-wall and smooth wall turbulent boundary layers. *Journal of Fluid Mechanics*, *108*, 363–382. https://doi.org/10.1017/S0022112081002164

Raupach, M. (1992). Drag and drag partition on rough surfaces. *Boundary-Layer Meteorology*, *60*(4), 375–395. https://doi.org/10.1007/BF00155203

Raupach, M., Thom, A., & Edwards, I. (1980). A wind-tunnel study of turbulent flow close to regularly arrayed rough surfaces. *Boundary-Layer Meteorology*, *18*(4), 373–397. https://doi.org/10.1007/BF00119495

Raus, D. (2019). *Transport sédimentaire sur rugosités immobiles: De l'hydrodynamique locale à la morphodynamique (doctoral dissertation)*. University of Toulouse. Retrieved from https://www.theses.fr/2018INPT0059

Raus, D., Moulin, F., & Eiff, O. (2019). The impact of coarse-grain protrusion on near bed hydrodynamics. *Journal of Geophysical Research: Earth Surface*, *124*(7), 1854–1877. https://doi.org/10.1029/2018JF004751

Rickenmann, D., & Recking, A. (2011). Evaluation of flow resistance in gravel-bed rivers through a large field data set. *Water Resources Research*, *47*(7), 1–22. https://doi.org/10.1029/2010WR009793

Rouzes, M., Moulin, F., Florens, E., & Eiff, O. (2019). Low relative-submergence effects in a rough-bed open-channel flow. *Journal of Hydraulic Research*, *57*(2), 139–166. https://doi.org/10.1080/00221686.2018.1478894

Sarkar, S., Papanicolaou, A., & Dey, S. (2016). Turbulence in a gravel-bed stream with an array of large gravel obstacles. *Journal of Hydraulic Engineering*, *142*(11), 04016052. https://doi.org/10.1061/(ASCE)HY.1943-7900.0001191

Scherer, M., Uhlmann, M., Kidanemariam, A., & Krayer, M. (2022). On the role of turbulent large-scale streaks in generating sediment ridges. *Journal of Fluid Mechanics*, *930*, A11. https://doi.org/10.1017/jfm.2021.891

Sechet, P., & Guennec, B. (1999). Bursting phenomenon and incipient motion of solid particles in bed-load transport. *Journal of Hydraulic Research*, *37*(5), 683–696. https://doi.org/10.1080/00221689909498523

Stradiotti, G., Righetti, M., Tarekegn, T., Wharton, G., & Toffolon, M. (2020). New conceptual framework for the erosion of fine sediment from a gravel matrix based on experimental analysis. *Journal of Hydraulic Engineering*, *146*(9), 04020061. https://doi.org/10.1061/(ASCE)HY.1943-7900.0001795

Sumer, B. (1986). Recent developments on the mechanics of sediment suspension. In W. Bechteler (Ed.), *Transport of suspended solids in open channel* (pp. 3–13). Euromech 196.

Tominaga, A., Nezu, I., Ezaki, K., & Nakagawa, H. (1989). Three-dimensional turbulent structure in straight open channel flows. *Journal of Hydraulic Research*, *27*(1), 149–173. https://doi.org/10.1080/00221688909499249

Tuijnder, A., Ribberink, J., & Hulscher, S. J. M. H. (2009). An experimental study into the geometry of supply-limited dunes. *Sedimentology*, *56*(6), 1713–1727. https://doi.org/10.1111/j.1365-3091.2009.01054.x

Vanderwel, C., & Ganapathisubramani, B. (2015). Effects of spanwise spacing on large-scale secondary flows in rough-wall turbulent boundary layers. *Journal of Fluid Mechanics*, *774*, 1–R2. https://doi.org/10.1017/jfm.2015.292

Vanderwel, C., Stroh, A., Kriegseis, J., Frohnapfel, B., & Ganapathisubramani, B. (2019). The instantaneous structure of secondary flows in turbulent boundary layers. *Journal of Fluid Mechanics*, *862*, 845–870. https://doi.org/10.1017/jfm.2018.955

Vericat, D., Batalla, R. J., & Gibbins, C. (2008). Sediment entrainment and depletion from patches of fine material in a gravel-bed river. *Water Resources Research*, *44*(11), W11415. https://doi.org/10.1029/2008WR007028

Wang, Z., & Cheng, N. (2006). Time-mean structure of secondary flow in open with longitudinal bedforms. *Advances in Water Resources*, *29*(11), 1634–1649. https://doi.org/10.1016/j.advwatres.2005.12.002

Wang, Z., & Cheng, N.-S. (2005). Secondary flows over artificial bed strips. *Advances in Water Resources*, *28*(5), 441–450. https://doi.org/10.1016/j.advwatres.2004.12.008

Wangsawijaya, D. D., Baidya, R., Chung, D., Marusic, I., & Hutchins, N. (2020). The effect of spanwise wavelength of surface heterogeneity on turbulent secondary flows. *Journal of Fluid Mechanics*, *894*, A7. https://doi.org/10.1017/jfm.2020.262

Westerweel, J., & Scarano, F. (2005). Universal outlier detection for PIV data. *Experiments in Fluids*, *39*(5), 1096–1100. https://doi.org/10.1007/s00348-005-0016-6

Wilcock, P., & McArdell, B. (1993). Surface-based fractional transport rates: Mobilization thresholds and partial transport of a sand-gravel sediment. *Water Resources Research*, *29*(4), 1297–1312. https://doi.org/10.1029/92WR02748

Willingham, D., Anderson, W., Christensen, K., & Barros, J. (2014). Turbulent boundary layer flow over transverse aerodynamic roughness transitions: Induced mixing and flow characterization. *Physics of Fluids*, *26*(2), 025111. https://doi.org/10.1063/1.4864105

Wolman, M., & Brush, L. (1961). Factors controlling the size and shape of stream channels in coarse noncohesive sands. In *Geological Survey Professional Paper, 282-G* (pp. 183–210).

Wren, D., Kuhnle, R., Langendoen, E. J., & Rigby, J. R. (2014). Turbulent flow and sand transport over a cobble bed in a laboratory flume. *Journal of Hydraulic Engineering*, *140*(4), 04014001. https://doi.org/10.1061/(ASCE)HY.1943-7900.0000838

Wu, W., & Wang, S. (1999). Movable bed roughness in alluvial rivers. *Journal of Hydraulic Engineering*, *125*(12), 1309–1312. https://doi.org/10.1061/(ASCE)0733-9429(1999)125:12(1309)

Yager, E., Kirchner, J., & Dietrich, W. (2007). Calculating bed load transport in steep boulder bed channels. *Water Resources Research*, *43*(7),W07418. https://doi.org/10.1029/2006WR005432

Zampiron, A., Nikora, V., Cameron, S., Patella, W., Valentini, I., & Stewart, M. (2020). Effects of streamwise ridges on hydraulic resistance in open-channel flows. *Journal of Hydraulic Engineering*, *146(1)*, 06019018. https://doi.org/10.1061/(ASCE)HY.1943-7900.0001647

Erratum

In the originally published article, the hyperlink for the reference Al-Awadhi (1999) in the References section did not work. In addition, in the third sentence of the fourth paragraph of Section 4.2, the range was incorrectly presented as "(0.5,0.9)" and has since been corrected to "[0.5,0.9)." These errors have been corrected, and this version may be considered the authoritative version of record.